

On the seismic response of deep-seated rock slope instabilities – Insights from numerical modeling



Valentin S. Gischig^{a,c,*}, Erik Eberhardt^a, Jeffrey R. Moore^b, Oldrich Hungr^a

^a Geological Engineering, Department of Earth, Ocean, & Atmospheric Sciences, University of British Columbia, Vancouver, Canada

^b Geology & Geophysics, University of Utah, Salt Lake City, USA

^c Swiss Competence Center for Energy Research – Supply of Energy (SCCER-SoE), Department of Earth Sciences, ETH Zürich, Switzerland

ARTICLE INFO

Article history:

Received 25 June 2014

Received in revised form 26 March 2015

Accepted 3 April 2015

Available online 15 April 2015

Keywords:

Seismic landslide hazard

Spectral amplification

Topographic amplification

Newmark method

ABSTRACT

Earthquake-induced landslides constitute a critical component of seismic hazard in mountainous regions. While many seismic slope stability analysis methods exist with varying degrees of complexity, details of interactions between seismic waves and incipient landslides are not well understood and rarely incorporated, in particular for deep-seated slope instabilities. We present a series of 2D distinct-element numerical models aimed at clarifying interactions between earthquakes and large rock slope instabilities. The study has two main goals: 1) to explore the role of amplification in enhancing co-seismic slope deformation – a relationship widely discussed in literature but rarely tested quantitatively; and 2) to compare our numerical results with the well-established Newmark-method, which is commonly used in seismic slope stability analysis. We focus on three amplification phenomena: 1) geometric (topographic) amplification, 2) amplification related to material contrasts, and 3) amplification related to compliant fractures. Slope height, topography, seismic velocity contrasts, and internal strength and damage history were varied systematically in a series of models with a relatively simple, scalable geometry. For each model, we compute the spatial amplification patterns and displacement induced by real earthquake ground motions. We find that material contrasts and internal fracturing create both the largest amplification factors and induced displacements, while the effect of geometry is comparably small. Newmark-type sliding block methods underestimate displacements by not accounting for material contrasts and internal fracturing within the landslide body – both common phenomena in deep-seated slope instabilities. Although larger amplification factors tend to be associated with greater displacements, we did not identify a clear link between ground motion frequency content, spectral amplification, and induced displacement. Nevertheless, observation of amplification patterns can play an important role in seismic slope stability analyses, as: 1) strong amplification (related to material contrasts or compliant fractures) is an indicator of potentially large co-seismic displacements; and 2) amplification patterns can be used to constrain geological and numerical models used for seismic stability analysis. The complexity of wave–slope interactions, as well as the potential to severely underestimate hazard using Newmark-type methods, motivates use of rigorous numerical modeling for quantitative seismic hazard and risk assessment of large landslides.

© 2015 Elsevier B.V. All rights reserved.

1. Introduction

Earthquake-induced landslides are among the most hazardous secondary effects of strong seismicity in mountainous regions, and a number of case histories highlight the potentially devastating consequences. The 2008 M_w 7.9 Wenchuan earthquake in China, for example, resulted in nearly 90,000 fatalities, of which an estimated 25–30% were caused by landslides (Huang et al., 2012; Huang and Fan, 2013). Twenty-three large landslides each killed at least 30 people (Yin et al., 2009), while 257 new landslide-dammed lakes threatened the safety of millions more (Cui et al., 2009). The 2005 M_w 7.6 Kashmir earthquake in

Pakistan similarly triggered several thousand landslides (Owen et al., 2008), killing an estimated 25,500 people – nearly 30% of the total number of fatalities attributed to the earthquake (Dunning et al., 2007). The largest was a rock avalanche with volume >80 million m^3 , which killed approximately 1000 people, buried four villages and dammed two lakes. The 2001 Las Colinas landslide in El Salvador (volume 130,000 m^3), triggered by the M_w 7.6 San Salvador earthquake, caused 585 fatalities and alone accounted for more than half of the total earthquake death toll (Evans and Bent, 2004; Crosta et al., 2005). Many other well-documented landslide disasters were also triggered by earthquakes, such as the Nevado Huascarán rock-ice avalanche, one of the deadliest landslides in history with more than 18,000 fatalities (Plafker and Ericksen, 1978), or the Madison Canyon landslide (Montana, USA), one of the largest in North America (Hadley, 1964).

* Corresponding author.

E-mail address: gischig@erdw.ethz.ch (V.S. Gischig).

Such cases highlight the pressing need to better understand the physics of co-seismic landslide triggering, and improve quantitative methods for seismic slope stability hazard assessment.

The significance of landslides as a component of earthquake hazard has long been recognized, as demonstrated by the vast body of literature on seismic slope stability modeling approaches. Jibson (2011) summarizes the most common methods to estimate co-seismic landslide hazard: they range from simple pseudo-static analysis to complex numerical simulation. A compromise in complexity between these two approaches is the Newmark sliding-block method (Newmark, 1965), which allows efficient computation of seismically-induced slope displacements from acceleration time histories. Newmark's approach – originally developed for earth dams and embankments – treats the landslide mass as a rigid plastic body (i.e. the mass does not deform internally) that slides on a plane of constant dip and friction. The method was later developed beyond the rigid-block assumption (see summary by Bray (2007)) with the aim of including eigenmode excitation of the potential sliding body. Jibson (2011) cautions that displacements obtained by all Newmark-type methods are estimates, and should be regarded as index values for evaluating landslide susceptibility. Due to the simplicity and efficiency of the method, it has proven powerful for regional studies aimed at delineating areas prone to co-seismic landslides (Jibson et al., 2000; Allstadt et al., 2013). However, it is known that such methods may only be valid for small landslide masses. Jibson (2011) suggests that if the first fundamental period of the landslide body is larger than one-tenth the mean period of ground motion (i.e. $T_s/T_m > 0.1$), compliant behavior of the landslide body must be considered (as in Bray and Travararou, 2007).

For stability analysis of large, deep-seated landslides (herein defined as volume $> 100,000 \text{ m}^3$), a simple index value representing seismic response may not provide adequate information to anticipate the probability of catastrophic failure. Jibson (2011) stresses that in case of communities or infrastructure (e.g., storage dams, highways, pipelines, crushers or conveyors in open pit mines, etc.) built on or in close proximity to landslides or in the area of potential catastrophic run-out more intense investigation is required. Detailed numerical modeling becomes appropriate when sufficient data are available describing landslide material properties and behavior, internal structure and kinematics, as well as displacement trends over time (Gischig et al., 2011a). These are in turn generated at a level of detail proportional to the associated hazard or risk. The capability of numerical methods to quantify co-seismic slope deformations has been demonstrated by a number of case history studies (e.g. Lenti and Martino, 2013; Bourdeau and Havenith, 2008; Danneels et al., 2008; Bozzano et al., 2008, 2011; Bhasin and Kaynia, 2004). Nevertheless, a routine strategy does not currently exist for performing seismic slope stability analyses with numerical methods that account for complexities of earthquake ground motion and slope deformation processes. Details and sensitivities of earthquake–slope interactions must first be explored systematically and key couplings identified.

The interaction between seismic waves and hill slopes is complex (Geli et al., 1988; Sepúlveda et al., 2005a). Sparse field data and observations (e.g., ground motion records on or close to seismically deforming slopes), however, provide only limited insights into wave–slope interaction phenomena. Sepúlveda et al. (2005a,b, 2010) highlight the importance of topographic amplification in controlling landslide patterns, while Ashford et al. (1997) and Geli et al. (1988) emphasize that eigenfrequency excitation and topographic amplification are difficult to distinguish. Del Gaudio and Wasowski (2011) attribute high importance to site amplification arising from velocity contrasts between the landslide body and underlying bedrock. They further note that the preferred orientation of amplification (i.e. directivity in site response) may be controlled by a combination of topographic, lithological and structural factors that together redistribute wave energy. Bourdeau and Havenith (2008) find that amplification relevant for landslide triggering mostly arises from geological site effects (i.e., seismic velocity contrasts between material layers), while topographic amplification plays a secondary role. Burjánek et al. (2010, 2012) report strong localized amplification and

polarization on fractured rock slopes, which are interpreted to be caused by highly compliant tension fractures (Moore et al., 2011). Levy et al. (2010) observe spectral peaks in noise records from a rock column separated from stable ground by an open tension crack, which they attribute to eigenmode vibration of the column.

Amplification phenomena reported in the literature can be separated into three groups: 1) geometrical effects (i.e. topography), 2) material contrasts, and 3) structural effects (compliant fractures). The latter two amplification phenomena may also be regarded as end members of a similar mechanism related to internal damage of unstable rock masses. In case (2), intense fracturing and deformation within the sliding body produces a bulk reduction of rock mass strength and stiffness (and thus seismic velocity), which results in velocity contrasts between the underlying or adjacent, less damaged material. In case (3), discrete large-scale fractures – especially when opened by extensional strain – define blocks that can vibrate with additional degrees of freedom, and thus produce local amplification at distinct frequencies. We envision a spectrum between these mechanisms, depending on fracture density and internal structure of an unstable rock mass. For instance, at the Randa rock slope instability in Switzerland (Gischig et al., 2011a), fracturing within the unstable body produces both velocity contrasts (Heincke et al., 2006) and localized amplification phenomena (Burjánek et al., 2010; Moore et al., 2011).

Multiple types of amplification can play a role in co-seismic landslide triggering. However, in-depth understanding of the details of wave–slope interactions, amplification phenomena, and landslide triggering does not currently exist. While direct field observations remain challenging, numerical methods are well-developed and able to offer new insights into earthquake–landslide interactions. Here we present a conceptual numerical study designed to clarify complex interactions between seismic waves and deep-seated rock slope instabilities. We explore the role of three amplification phenomena: 1) geometric effects (i.e. slope height and topography), 2) material contrasts, and 3) internal fracturing due to degraded rock mass strength or preconditioning through previous seismic loading. For each model, we compute spatial amplification patterns as well as displacements induced by real earthquake ground motions, with the goal of understanding the relationship between amplification and seismically-induced permanent slope deformation. Well aware that deep-seated landslides are structurally complex, our conceptual slope geometry is kept as simple as possible for three reasons: 1) to be able to distinguish effects of the three aforementioned amplification phenomena, 2) to allow comparison of displacements to those estimated from established Newmark-type methods, and 3) to allow geometric scaling in order to study scale effects on co-seismic displacement and amplification and separate these from other factors. We conclude by discussing relationships between amplification and slope deformation and elaborate on possible implications for seismic landslide hazard analyses.

2. Methods

2.1. UDEC model

Numerical modeling of earthquake-induced displacements was performed using the 2D distinct-element code UDEC (Itasca, 2011; Cundall and Hart, 1992). The strength of this code is its ability to explicitly include discontinuities and model large dislocations. Discontinuities cut the medium into an assemblage of blocks, which are connected by springs that mimic fracture compliance in both normal and shear. Discontinuities are also assigned a failure criterion (Coulomb slip with tensile cut-off in our case), which governs the onset of permanent dislocation. Blocks bounded by discontinuities are discretized with a triangular mesh, for which a finite-difference scheme is solved to account for block deformations. Blocks in our study were assigned a purely elastic constitutive law (i.e., deformable but failure not permitted) for simplicity.

UDEC also has the capability to accurately model wave propagation and account for damping due to frictional energy loss. Rayleigh damping is implemented where damping is proportional to mass and stiffness (Itasca, 2011). Rayleigh damping is generally frequency-dependent, but can be approximated as frequency-independent around a center frequency f_{min} . Hence, for dynamic analysis damping must be chosen such that it is realistic in the frequency range of interest. Two parameters govern damping in the model, the center frequency f_{min} , and damping factor ξ_{min} , where f_{min} is the frequency at which damping is minimal, while ξ_{min} is the fraction of critical damping. Following the guidelines of Itasca (2011), ξ_{min} was set to a small value, 0.005 in our case, while f_{min} was set to 2 Hz, meaning that damping was minimal between 1 and 4 Hz. Outside this interval, damping increases. We are interested in frequencies between about 0.1 and 10 Hz, because the dominant frequency content of large earthquakes lies within this range (e.g. Bourdeau and Havenith, 2008; Del Gaudio and Wasowski, 2011). By setting damping to a low value, damping across the entire frequency range of interest was minimal.

A key consideration for dynamic analysis is sufficiently fine discretization to avoid adverse effects (such as aliasing) on wave representation in the frequency range of interest. Kuhlemeyer and Lysmer (1973) suggest that the minimum mesh size must be smaller than 1/10 to 1/8 of the minimum wavelength (i.e. of the highest frequency) of the input motion. For our UDEC modeling, the lowest seismic velocity across all models was $V_S = 1254$ m/s, although in most cases the lowest seismic velocity was $V_S = 2172$ m/s. Hence, in order to accurately represent waves up to 10 Hz, we discretized a wave length of about 125 m (or 220 m, respectively) by ten node points. Thus, we chose a maximum mesh size of approximately 12 m (or 20 m, respectively).

To avoid adverse boundary effects, such as reflections at the side and bottom of our model, we used absorbing boundary conditions. At the lateral boundaries, a free-field boundary condition was applied, which mimics an infinite continuum. At the base of the model, we assigned viscous boundary conditions (i.e. dash pots in the normal and shear direction). These require that basal input motions be converted into stress boundary conditions, calculated as:

$$\begin{aligned}\sigma_n(t) &= 2\rho V_P v_n(t) \\ \sigma_s(t) &= 2\rho V_S v_s(t)\end{aligned}\quad (1)$$

where σ_n and σ_s are the time-dependent normal and shear stresses at the bottom boundary, V_P and V_S are the P- and S-wave velocities, respectively, v_n and v_s are the instantaneous vertical and horizontal velocity input motions, and ρ is the material density (Itasca, 2011). We only apply horizontal components of velocity input motions to allow direct comparison with Newmark methods.

Fig. 1a shows the model geometry used in our study. For reasons given earlier, we selected a simple, scalable slope configuration amenable to comparisons with the Newmark method. The slope consists of a 60° dipping face with variable height, and a 25° dipping basal sliding surface with a friction angle of 30°. For the model sequence that focuses on internal deformation, we added a network of potential (incipient) fracture pathways using a Voronoi tessellation scheme (Itasca, 2011). The strength of these incipient pathways was assigned intact rock properties; i.e., a constant friction angle of 40°, with variable cohesion and tensile strength values that drop to zero residual strength after peak strength is exceeded, while the friction angle remains constant. Table 1 lists material properties used in our model, including those that were varied in sensitivity analyses. Note that the assumed elastic modulus of 30 GPa corresponds to a stiff rock mass, for example granitic rock with an intact modulus of 90 GPa, GSI of 50, and disturbance factor of $D = 0$ (Hoek and Diederichs, 2006). This rock mass elastic modulus is on the higher end of likely landslide material, and allows for enhanced computation speed. Smaller modulus values would require finer discretization.

Before performing dynamic analyses, an initial in-situ stress state was assumed and the model solved to equilibrium. For this, we assigned stress boundary conditions with gravity loading and $K = 1$ (i.e., $\sigma_{xx} = \sigma_{zz} = \rho g \Delta z$, $\sigma_{xz} = 0$). For the out-of-plane stresses, the plane-strain assumption is used. Note that it is important to initiate in-situ stresses with stress boundary conditions rather than displacement boundaries, since the free-field boundaries used in our dynamic analyses correspond to stress boundary conditions.

2.2. Computation of amplification characteristics

Amplification patterns were computed adapting the methodology used by Bourdeau and Havenith (2008) and Lenti and Martino (2012, 2013) based on Ricker wavelets as input motions. Ricker wavelets are commonly used in studies of eigenmode vibration due to their short time duration and well-defined spectral content around a dominant frequency. The choice of Ricker wavelet input motions is not critical for our results, however, as other input motions (e.g. an impulse band-pass filtered in frequency range of interest) would yield similar results. The analytic expression of a Ricker wavelet in the time domain is:

$$v_R(t) = A \left(1 - 2\pi^2 f_{dom}^2 (t-1)^2 \right) e^{-\pi^2 f_{dom}^2 (t-1)^2} \quad (2)$$

where A is the amplitude and f_{dom} is the dominant frequency. The spectrum of $v_R(t)$ has a maximum amplitude at f_{dom} . An example Ricker wavelet with $f_{dom} = 1$ Hz is shown in Fig. 1b and c. To determine slope amplification patterns in the frequency range of 0.1–10 Hz, we used a sequence of Ricker wavelets with different dominant frequencies $f_{dom} = 0.25, 0.5, 1, 2, 4,$ and 8 Hz as input motions in UDEC. We then computed amplification as the ratio of the spectra of waveforms at the model surface to the spectrum of the input Ricker wavelet (i.e., at the bottom boundary). Finally, a combined spectral amplification curve $A(f)$ was computed from the amplification curve derived for each Ricker wavelet frequency f_{dom} .

$$A(f) = \frac{\sum_R C_R(f) A_R(f)}{\sum_R C_R(f)} \quad (3)$$

R represents the Ricker wavelets with $f_{dom} = 0.25, 0.5, 1, 2, 4,$ and 8 Hz. This represents a weighted average of six amplification curves $A_R(f)$, where the amplification factor at each frequency is weighted by the spectral amplitude $C_R(f)$ of the corresponding input wavelet R . We computed spectral amplification curves for dense observation points spaced at ~ 10 m, and present amplification as a function of space and frequency (for an example see Fig. 3a, b: ground surface, and c, d: sliding surface).

Note that in a homogeneous half-space, the spectral ratio of a wave observed at a free surface to the wave traveling towards the free surface is two, due to the free-surface effect (i.e., superposition of the incident and reflected waves doubling the amplitude at the surface). Thus for amplification curves computed at the surface, spectral ratios between observation points and the basal input motion were divided by two. In contrast, amplification curves from within the landslide body (e.g., along the sliding surface) were not halved, because these generally do not include free-surface effects.

2.3. Input ground motions

Real earthquake ground motions were used in our study, taken from the database in the software package SLAMMER (provided by the USGS; Jibson et al., 2013). Sensitivity of our model results was tested against the seven input motions shown in Table 2 and Fig. 2. These were selected to cover a wide range of possible mean frequencies, f_m , spanning 1.3–5.9 Hz, and epicenter distances from 5 to 50 km. All of these ground

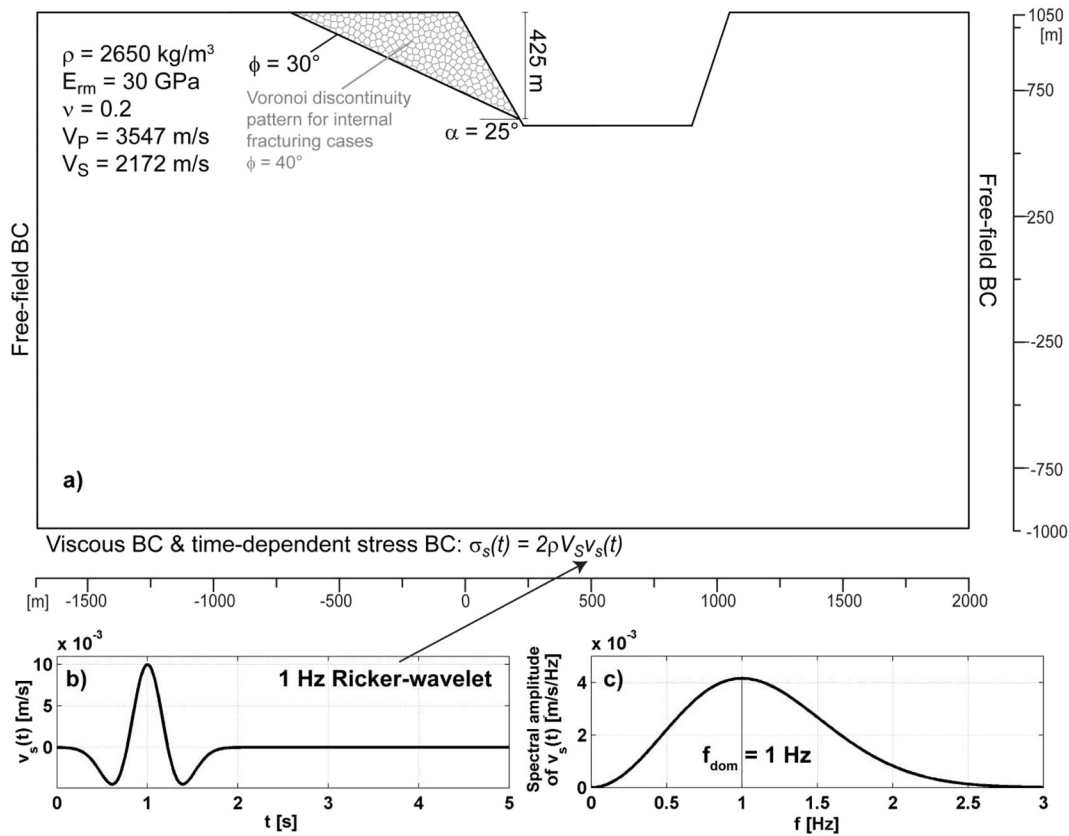


Fig. 1. a) Geometric boundary conditions and material properties used for dynamic analysis in UDEC. ρ is rock mass density, E_{rm} is Young's modulus of the rock mass, ν is Poisson's ratio. V_P and V_S are P- and S-wave velocities, respectively, ϕ is the friction angle. b) Example of a Ricker wavelet with dominant frequency of 1 Hz as used to compute amplification patterns. c) Corresponding Fourier spectrum of the 1 Hz Ricker wavelet.

motions do not necessarily correspond to recordings from rock slope sites, as would be most realistic for slope stability analysis. We also include recordings that are potentially affected by site effects (e.g. EQ4–EQ7), as can be seen from the long low-frequency codas. These were nevertheless included to enhance ground motion variability so that

our sensitivity analysis is as broad as possible. f_m was computed in analogy to Bray and Rathje (1998):

$$f_m = \frac{\sum_i C_i^2 f_i}{\sum_i C_i^2} \quad (4)$$

Table 1

Material properties; values in parentheses indicate the range over which properties were varied in our sensitivity study.

Rock mass	
Density, ρ [kg/m ³]	2650
Young's modulus [GPa]	30 (10–90)
Poisson's ratio	0.2
P-wave velocity V_P [m/s]	3547
S-wave velocity V_S [m/s]	2172
Sliding surface	
Friction angle, ϕ [°]	30
Cohesion [MPa]	0
Tensile strength [MPa]	0
Residual cohesion [MPa]	0
Residual tensile strength [MPa]	0
Fracture normal stiffness [GPa/m]	10
Fracture shear stiffness [GPa/m]	5
Voronoi discontinuities	
Friction angle, ϕ [°]	40
Cohesion [MPa]	Variable (2, 5, 10, 15)
Tensile strength [MPa]	Variable (0.2, 0.5, 1, 1.5)
Residual cohesion [MPa]	0
Residual tensile strength [MPa]	0
Fracture normal stiffness [GPa/m]	10
Fracture shear stiffness [GPa/m]	5

where C_i is the Fourier amplitude at frequency f_i . We acknowledge that this parameter does not fully describe the details of ground motion frequency content. In particular, peak spectral acceleration may occur at a frequency up to 2 Hz different than f_m (Fig. 2). However, the f_m parameter helped selecting ground motions with widely varying frequency content. Further, we used it to be able to examine the sensitivity of slope response to ground motion frequency content in the same way as done by Bray and Rathje (1998) and Bray and Travararou (2007). Note that they used the mean period T_m , not the mean frequency f_m , (computed analogous to Eq. (4)) to characterize frequency dependent slope response.

For comparison with Newmark-type methods, 150 ground motions were recovered from the SLAMMER database. Only recordings with epicenter distances of <70 km were used. We arbitrarily selected only one horizontal component per recording. Most chosen recordings are from locations involving rock (site class A: rock, $V_S > 600$ m/s or <5 m of soil over rock). To increase the variability of the ground motions, and to obtain a sufficient number of ground motions for our analysis, a few recordings from shallow stiff soils were also included (site class B: shallow stiff soil less than 20 m thick overlying rock). To allow comparison of our results to Newmark-type methods, we applied each input motion to our model in the horizontal direction; i.e., we did not include the vertical component of ground motion. Displacements from Newmark

Table 2

Earthquake ground motions used in our study; taken from SLAMMER (Jibson et al., 2013). Abbreviated parameters are M : magnitude, f_m : mean frequency, and D_e : epicentral distance.

Earthquake, year	Station-component	M	PGA [g]	f_m [Hz]	D_e [km]	Focal mechanism
EQ1	Cape Mendocino, 1992	7.1	0.19	5.9	36.3	Reverse
EQ2	Chi-Chi, 1999	7.6	0.96	4.1	14.2	Oblique reverse
EQ3	Northridge, 1994	6.7	0.99	3.1	5.4	Reverse
EQ4	Morgan Hill, 1984	6.2	0.22	2.8	37.3	Strike-slip
EQ5	Cape Mendocino, 1992	7.1	0.18	1.7	53.3	Reverse
EQ6	Northridge, 1994	6.7	0.61	1.4	13.1	Reverse
EQ7	Northridge, 1994	6.7	0.33	1.3	21.6	Reverse

methods were computed using SLAMMER. Both rigid-block analysis (Jibson, 2011) and the coupled approach based on one-dimensional modal analysis (Rathje and Bray, 1999), were performed.

3. Geometric effects

3.1. Slope height

We begin by investigating the sensitivity of predicted amplification patterns to the scale of the instability, varied by changing the modeled slope height. Many authors (e.g. Bray and Travararou, 2007; Rathje and Bray, 1999) have proposed that slope height is an important factor affecting earthquake-triggered landslides. We selected a slope geometry with minimal average relief (i.e., flat topography behind the crest

and in front of the toe; Fig. 1) to limit topographic effects, which are explored later in Section 3.1.2.

3.1.1. Amplification

Fig. 3 shows predicted amplification patterns for a 75 m and 425 m high slope, both at the ground surface (Fig. 3a and b) and along the sliding plane (Fig. 3c and d). Amplification patterns at the ground surface correspond to those that may be measured from field surveys (e.g., Danneels et al., 2008). However, amplification along the sliding surface may be more relevant for understanding landslide triggering, as shear localization along the failure plane accommodates landslide displacement. Recall that amplification at the ground surface is halved to compensate for the free-surface effect, while this is not done for amplification along the sliding surface.

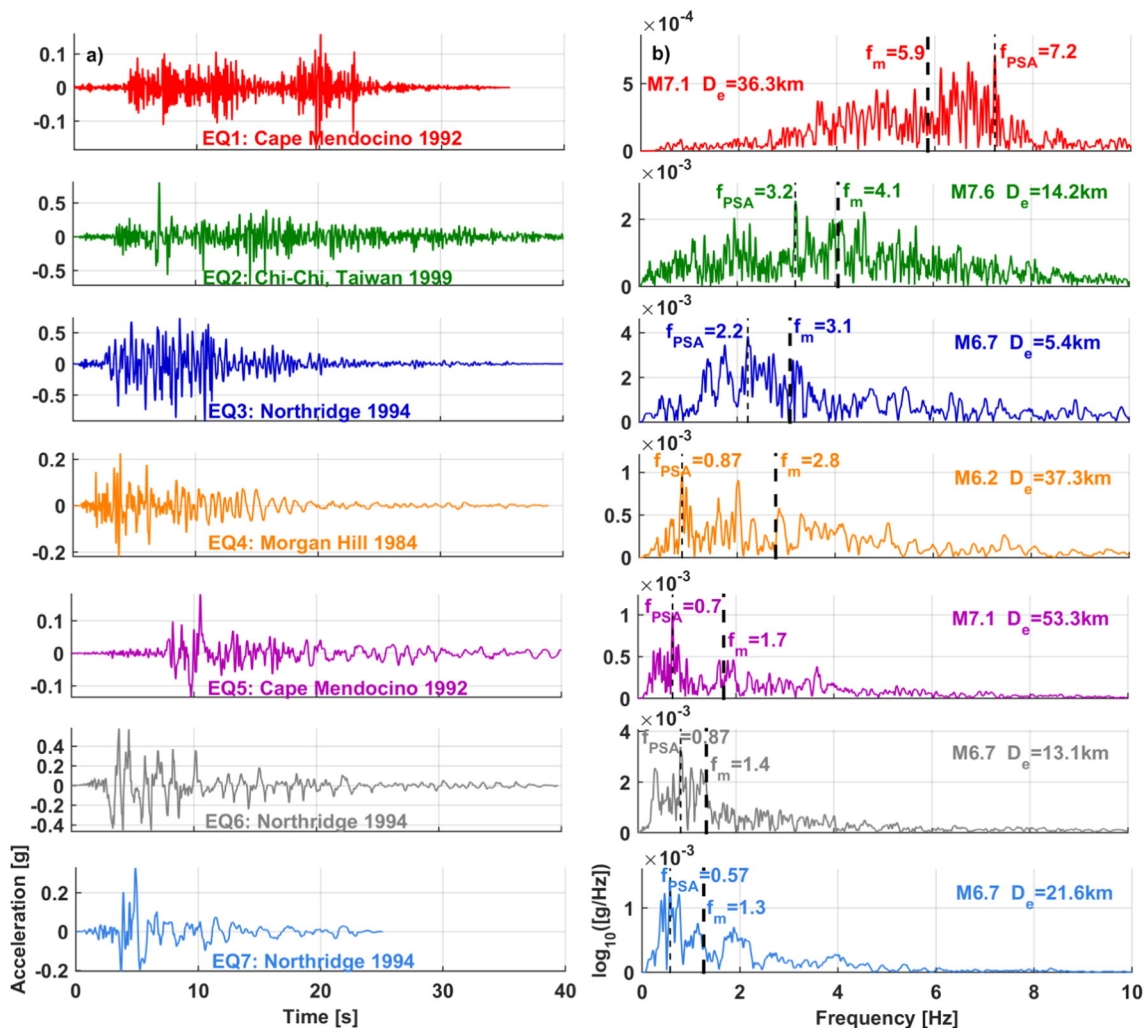


Fig. 2. a) Input ground motions used to compute co-seismic displacements in Figs. 4, 5b, 7, 9a, and 12a. b) Corresponding Fourier spectra. Also indicated is the mean frequency f_m and frequency at peak spectral amplification f_{PSA} .

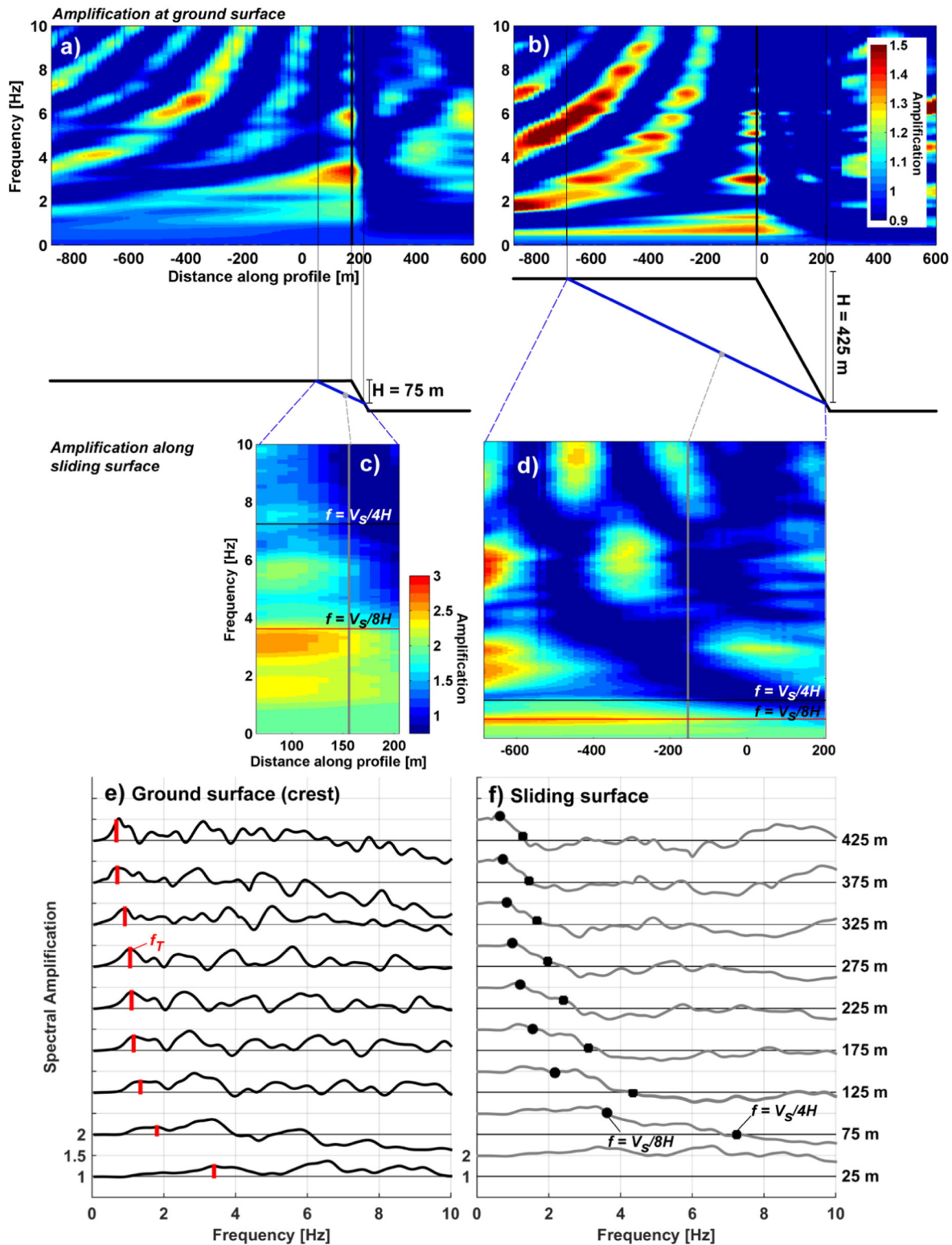


Fig. 3. a) Amplification pattern at the ground surface of a 75 m high slope. Each vertical trace along the profile corresponds to the spectral amplification curve of an observation point. These are distributed at a spacing of ~10 m along the ground surface. Note that amplification is divided by 2 to correct for the free-surface effect. b) Amplification pattern at the ground surface of a 425 m high slope. c) Amplification along the sliding surface of the 75 m high slope. Note in this case amplification was not halved since observation points are not on the free surface. d) Amplification pattern along the sliding surface for the 425 m slope. e) Spectral amplification at the slope crest, see thick black line in a) and b), where amplification factors tend to be greatest, for slope heights ranging from 25 m to 425 m. Highlighted in red is the frequency of the first amplification peak termed topographic frequency. f) Spectral amplification at one point along the sliding surface, see gray line in c) and d). (For interpretation of the references to color in this figure legend, the reader is referred to the web version of this article.)

For both the 75 and 425 m high slopes, the strongest ground-surface amplification occurs at the crest (Fig. 3a and b). For the 425 m high slope, local amplification reaches a maximum value of 1.6, with several

maxima. Fig. 3e presents spectral amplification curves from the slope crest (i.e. where amplification is strongest) for nine different slope heights ranging from 25 m to 425 m in 50 m increments. Results

show that the frequency of the first amplification maximum is inversely correlated with slope height, varying from 0.75 Hz for the 425 m high slope to 1.9 Hz for the 75 m high slope. Amplifications at those frequencies involve the entire slope (Fig. 3a and b). In analogy with Ashford et al. (1997), we refer to this as the topographic frequency, f_T , which is indicated by the red bars in Fig. 3e. Topographic amplification factors increase slightly with increasing slope height, reaching a maximum value of 1.37 for the 425 m high slope. Amplification patterns – in particular those at higher frequencies – do not change systematically for different slope heights, but instead exhibit complex patterns as in Fig. 3a and b.

Amplification along the length of the sliding surface occurs at low frequencies (Fig. 3c and d). At frequencies less than $f = V_s/8H$, amplification is >2 along the entire sliding plane. Also shown in Fig. 3 is the frequency $f = V_s/4H$, above which amplification patterns become more complex and localized. Note that these two frequencies correspond to a wavelength eight and four times larger than the slope height. Amplification curves for all slope heights are extracted for the point closest to the crest (gray marker and line in Fig. 3), and presented in Fig. 3f. At frequencies less than $f = V_s/8H$, amplification ratios are two or greater, while at higher frequencies, amplification decreases until it reaches ~ 1 at around $f = V_s/4H$. At even higher frequencies, amplification patterns become considerably complex, with amplification and de-amplification resulting from complex wave interference. Amplification by a factor of two at wavelengths larger than eight times the slope height is a result of the free-surface effect penetrating into the rock mass for some portion of the wavelength. Positive interference of incoming and reflected waves is not only limited to the free surface, but reaches depths of about 1/8 to 1/4 of the wavelength. Note that little correlation between amplification peaks at the surface and along the sliding plane is apparent. Amplification at depth may thus not be simply deduced from amplification observed at surface.

The complex spectral amplification patterns shown in Fig. 3 arise from: 1) superposition of incident S-waves, reflected S- and P-waves, and Rayleigh waves created at the free surface; and 2) eigen-mode vibration of the slope (Bourdeau and Havenith, 2008; Ashford et al., 1997; Geli et al., 1988). It is not possible to decompose these two components of the wavefield. In particular, the fundamental frequency of the slope cannot be deduced from the topographic frequency, f_T , i.e., the first amplification maximum. The topographic frequency f_T for a 425 m high slope is 0.75 Hz. This differs from the topographic frequency suggested by Ashford et al. (1997), which is $V_s/5H = 1.02$ Hz. Bray (2007) assumed that the fundamental frequency (first resonant frequency) of a landslide body can be computed as follows: $f_s = V_s/4H$, where H is the slope height, or $f_s = V_s/2.6h$ for triangular shaped bodies, where h is the distance from the slope crest to the sliding surface. These frequencies would correspond to 1.28 and 1.97 Hz, respectively. We did not identify agreement between our f_T (or even amplification peaks at higher frequencies) and the expressions of Ashford et al. (1997) and Bray (2007) for any of the slope heights investigated. The contribution of fundamental-mode excitation to amplification is concealed by amplification effects from body and surface wave interactions, as suggested by Geli et al. (1988).

3.1.2. Displacements

Modeled displacements (from UDEC) induced by the seven selected ground motions in Fig. 2 are shown in Fig. 4a for slope heights ranging from 25 to 425 m (again in increments of 50 m). Displacements span more than three orders of magnitude ranging from a few millimeters (EQ1) to more than 2 m (EQ3 and EQ6). Displacements predicted as a function of slope height show strongly variable patterns for the different earthquakes: they are nearly constant in two cases (EQ6, EQ7), increase with slope height in two cases (EQ1 and EQ5), and decrease with slope height in three cases (EQ2, EQ3, and EQ4). The most extreme values are a factor of 4 decrease for EQ2 and factor of 2 increase for EQ5 at increasing slope heights. Note that the curves in Fig. 4 represent the maximum displacement of the entire displaced block. The range between

minimum and maximum displacement is also included as a shaded band. The range of displacements becomes particularly clear at small displacement values, where the toe of the slope has begun sliding before the back of the body has permanently displaced.

The variability in patterns of seismically-induced displacements versus slope height shown in Fig. 4a may arise from the different frequency content of the earthquake ground motions in relation to the amplification characteristics of the slopes. To search for a systematic relationship between frequency content and amplification characteristics on the one hand, and seismically-induced displacements on the other hand, we plot displacement versus amplification at the frequencies f_m and f_{PSA} (i.e. $A(f_m)$ and $A(f_{PSA})$) in Fig. 4b–e. f_{PSA} is the frequency corresponding to the peak of the acceleration spectrum (Peak Spectral Acceleration, PSA). In Fig. 4b and c, the amplification values are taken from the crest (i.e. from the curves in Fig. 3e), whereas in Fig. 4d and e, amplification is extracted from the sliding surface (Fig. 3f). Systematic correlation between amplification at these frequencies and displacements cannot be resolved. In particular, correlation is entirely absent between displacement and $A(f_m)$ at the crest. For $A(f_{PSA})$ at the crest a clear correlation can only be found for EQ5. A better correlation, although not always consistent, is found between $A(f_m)$ and $A(f_{PSA})$ along the sliding surface for EQ2 and EQ3. However, the correlation for EQ5 between displacement $A(f_{PSA})$ at the crest is contradictory for $A(f_m)$ along the sliding surface. Hence, neither amplification characteristics at the ground surface nor along the sliding surface are able to conclusively predict changes in displacement for different slope heights.

3.2. Topography

We investigate the role of topography by keeping the slope height and location of the sliding surface constant, but enhancing relief in a series of five models (Fig. 5). Fig. 5a shows amplification patterns for the steepest relief (line 5 in Fig. 5a). While the amplification patterns are similar as for the weakest topography (Fig. 3b, line 1 in Fig. 5a), amplification factors increase. Along the crest, the first amplification peak occurs at the same frequency ($f_T = 0.75$ Hz) as for the flat topography, but amplification factors increase from 1.5 (flat top) to about 2.5 (steepest topography). However, not only do distinct frequencies become further amplified, but amplification factors increase across the entire frequency band. For the steepest topography, amplification is greater than 1.5 between 0.5 and 7 Hz. Displacements increase gradually for all ground motions as topography steepens, however, only by a factor of 1.1 to 1.6.

4. Material contrasts

Many past studies have emphasized the role of material property contrasts in generating localized effects relevant for co-seismic landslide triggering (e.g. Del Gaudio and Wasowski, 2011; Bourdeau and Havenith, 2008; Danneels et al., 2008). Such contrasts may arise from a change in lithology (e.g. as described by Bourdeau and Havenith, 2008), or from increased fracturing and disturbance of a landslide body as compared to adjacent stable bedrock (e.g. landslides that have undergone large deformation; e.g. Bonzanigo et al., 2007). Here, we explore effects of a seismic velocity contrast between unstable and surrounding stable material by varying the elastic modulus of underlying bedrock between 10 and 90 GPa, while retaining a constant value of 10 GPa for the sliding block of the 425 m high slope. This strategy was chosen to explore the role of velocity contrasts while not changing elastic properties, and thus seismic velocity, of the unstable block. The modeled velocity interface occurs at the sliding surface; S-wave velocity contrasts between stable and unstable material ranged from 1 to 3. Note that velocity contrasts in natural settings may be greater than 3, as reported by Bourdeau and Havenith (2008), Heincke et al. (2006), and Heincke et al. (2010). The explored slope configuration may correspond to either: 1) an undisturbed slope experiencing first-time failure with a change in lithology along the potential sliding surface, or 2) a pre-

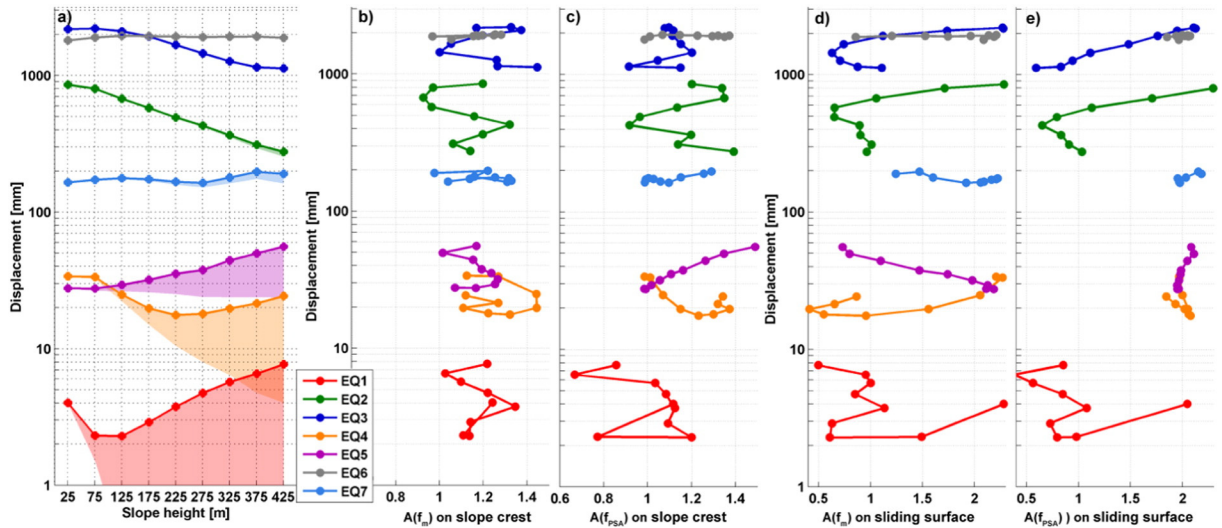


Fig. 4. a) Maximum displacement of the sliding block (thick line) induced by the seven earthquake ground motions in Fig. 2. Shading indicates the range between maximum and minimum displacements within the sliding block. b) Displacement versus amplification at frequency f_m , extracted at the slope crest. c) Displacement versus amplification at frequency f_{psa} (i.e. at the frequency of the peak spectral acceleration) extracted at the slope crest. d) and e) Same as a) and b) except that amplification is extracted from the point along the sliding surface also shown in Fig. 3f.

existing landslide, in which the stiffness of the sliding body is reduced due to long-term deformation.

4.1. Amplification

Modeled amplification patterns along the ground surface and sliding plane are shown in Fig. 6 for the two most extreme cases, i.e. with no velocity contrast (Fig. 6a and c), and for a velocity contrast of 3 (Fig. 6b and d). Amplification maxima in the latter case are concentrated within the sliding body and form a characteristic pattern of mostly positive interference between waves reflected at the surface and at the velocity contrast interface. Amplification patterns along the sliding plane also change for high velocity contrasts. The amplification patch seen at lowest frequencies, which persists along most of the sliding surface, includes a wider frequency range. It is not just limited to frequencies $< V_s/4H = 0.74$ Hz, but persists up to 2 Hz. Note that again the amplification pattern along the sliding plane does not resemble that at the ground surface (as in Fig. 3). The amplification factor at $f_T = 0.4$ Hz is at minimum 1.5 for the slope

without velocity contrast (as in Fig. 3c and d), and reaches a value of 6.3 at $f_T = 1.3$ Hz for a velocity contrast of 3. Maximum modeled amplification is > 7 at ~ 4 Hz.

4.2. Displacements

The sensitivity of predicted displacements to simulated velocity contrasts is shown in Fig. 7. Displacements generally increase with increasing velocity contrast. Only for EQ5 do displacements remain nearly constant. The strongest change in displacement occurs for EQ2 and EQ3, for which displacements increase by a factor of 5.5 and 4, respectively. For the other input motions, displacements increase by a factor of approximately 2. Although the general increase in amplification across the frequency spectrum is reflected in the overall increase of displacements, it is not obvious why displacements are nearly constant for EQ5 but increase for EQ6 and EQ7, because all three ground motions have similar frequency content dominant at < 2 Hz.

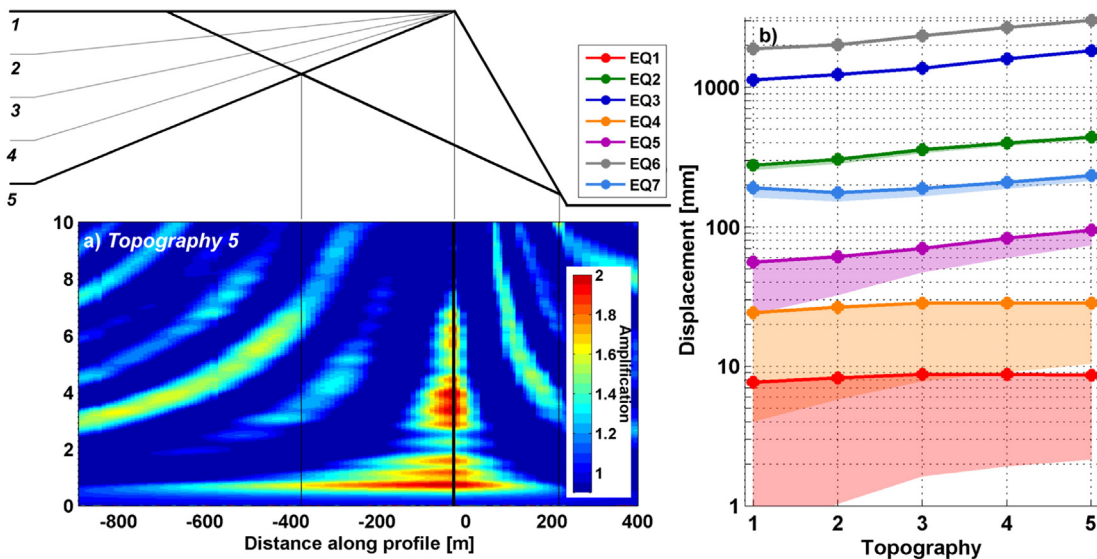


Fig. 5. Sensitivity to changing topography. a) Amplification at the ground surface with maximum topography (topography 5). b) Displacement induced by the ground motions in Fig. 2 for the five different topographies.

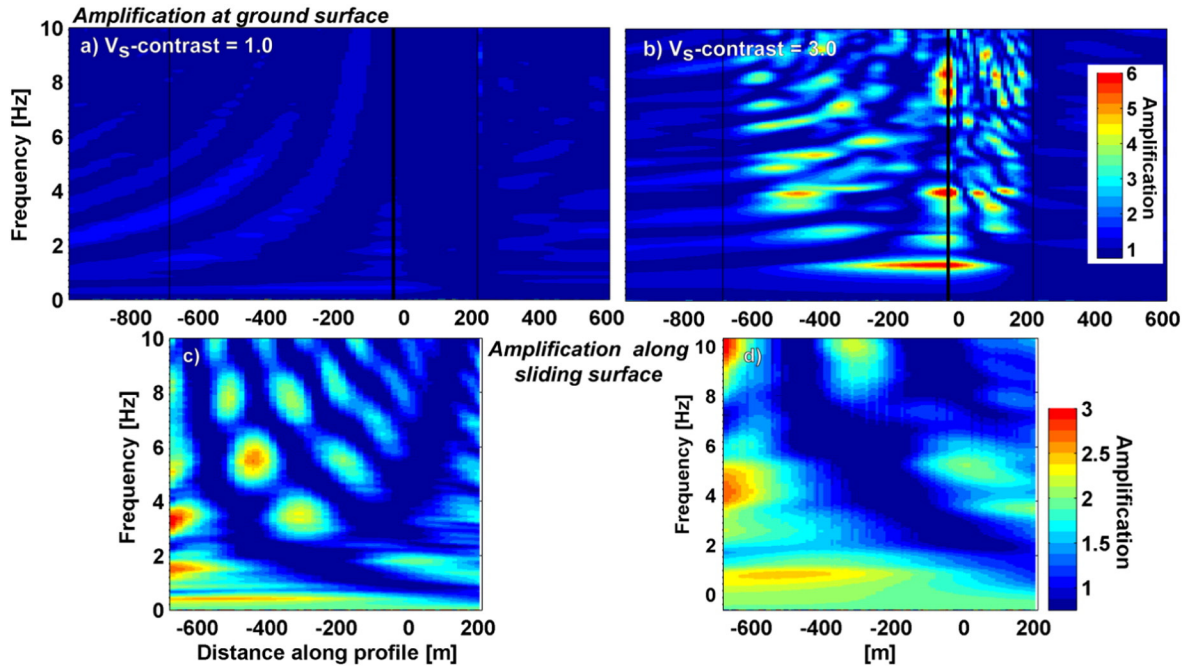


Fig. 6. a) Amplification at the ground surface for a 425 m high slope without seismic velocity contrasts. Note this does not correspond to Fig. 3b. Shear wave velocity V_S in this slope is 1254 m/s ($E = 10$ GPa), while in Fig. 3b it is 2172 m/s ($E = 30$ GPa). b) Amplification at the ground surface for a slope with three-times lower shear wave velocity in the sliding block as compared to the surrounding bedrock. c) and d) Corresponding amplification patterns along the sliding surface.

5. Internal fracturing

Here we explore the role of internal deformation and fracturing on interactions between seismic waves and a developing landslide. Models described previously neglected internal fracturing, in the interest of simplicity, which is not realistic for deep-seated rock slope instabilities. Even in cases such as the Tsaoling landslide (Chigira et al., 2003), which slid on a planar surface with translational kinematics, internal fracturing was observed and likely aided mobilization. The relevance of internal

fractures in generating localized effects within deep-seated instabilities has been highlighted by Burjánek et al. (2010, 2012) and Moore et al. (2011), who report strong spectral amplification and polarization caused by steeply-dipping and persistent, open cracks.

We added discontinuities to our unstable block (of 425 m height) in order to allow slip along fractures and fracture opening. Discontinuities included in our model represent incipient fractures (potential fracture pathways) and are based on a Voronoi tessellation procedure (Itasca, 2011; Fig. 1). The result is a network of polygonal blocks bounded by discontinuities with a wide range of orientations. Hence, failure is allowed to develop through propagation of fractures in a generally unrestricted manner.

5.1. Internal strength

In a first experiment, we explored the effect of decreasing discontinuity strength. We assigned a constant friction angle of 40° to all Voronoi discontinuities, and cohesion in different models of 15, 10, 5, and 2 MPa. Tensile strength was set to 1/10th of the cohesion. Once the peak strength along a discontinuity was exceeded, the residual cohesion and tensile strength dropped to zero.

5.1.1. Amplification

In Fig. 8, we show the slope geometry together with failed discontinuities and amplification patterns at the ground surface. Fractures within the block begin to form after initialization of gravitational loading, but the overall slope remains stable. For cohesion of 15 MPa, only part of the sliding surface slips, and a few discontinuities in the toe area fail (Fig. 8a). At cohesion of 10 MPa or less, tension cracks develop behind the slope crest. As soon as tension cracks form, amplification patterns at the ground surface become discontinuous. With a single tension crack (Fig. 8b), amplification characteristics change only marginally; new amplification peaks occur near the tensile fracture and along the slope crest at frequencies >5 Hz. Along the crest, the first amplification peak (at 1.25 Hz) increases slightly from a factor of 1.5 to 1.6. When three larger tension cracks develop (Fig. 8c), stronger amplification factors of around 2 occur at 4 to 5 Hz in the blocks between cracks. In the

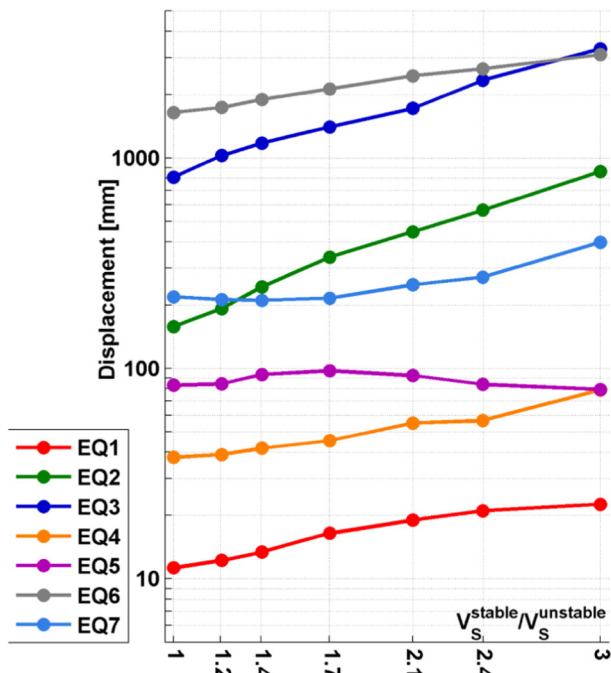


Fig. 7. Displacement induced by seven ground motions (Fig. 2) for varying seismic velocity contrasts.

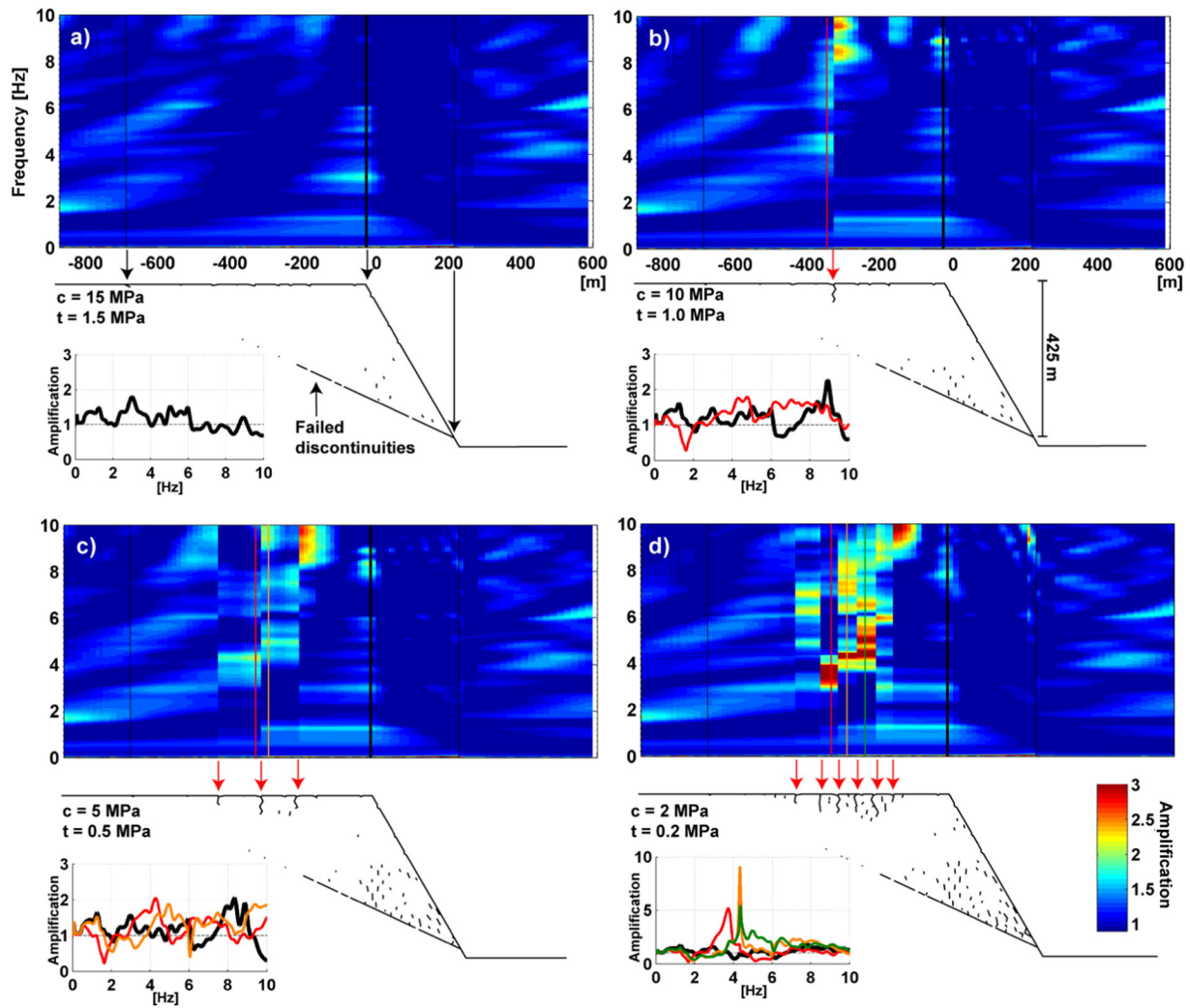


Fig. 8. Results of models exploring internal fracturing along Voronoi patterns of discontinuities (gray lines in Fig. 1). For each case of fracture cohesion and tensile strength, amplification patterns along ground surface are shown at top, while fractures that failed under initial gravitational loading are shown below. Also shown is the spectral amplification curve at the slope crest (black line), and at different blocks separated by tension fractures.

weakest model (Fig. 8d), several tension cracks develop with depths of up to 100 m. Along the surface where blocks are separated by these cracks, strong amplification factors of 5 to 9 occur at distinct frequencies. These results are in good agreement with recent measurements of ambient noise within slope instabilities; amplification factors reported by Burjánek et al. (2010, 2012) reach up to 10 at distinct frequencies within blocks bounded by open tension cracks. Modeled amplification along the slope crest is not as sensitive to crack development, and spectral amplifications below ~ 4 Hz show only minor change (Fig. 8).

5.1.2. Displacements

In Fig. 9, we show maximum displacements and the range of displacements within the sliding body (delineated by shading), for each of the input earthquakes in Fig. 2. As a general trend, displacements increase with decreasing discontinuity strength. The range between maximum and minimum displacement shows that the displacement field is more heterogeneous than for the intact block (cf. Fig. 4a). Deformation within the sliding body is considerable, and thus differences between maximum and minimum displacements can reach up to an order of magnitude. EQ7 shows the largest impact of decreasing strength with displacements undergoing a 10 fold increase. Fig. 9b and c displays two examples of earthquake-induced displacement and damage for models with only 2 MPa cohesion. For EQ1, the maximum displacement of 20 mm occurs at the toe, where shear stresses are most critical along

the sliding surface, while for EQ6, the maximum displacement of nearly 8 m occurs at the slope crest. In the latter case, most fractures within the sliding block have failed as a result of strong ground motion.

5.2. Role of open tension cracks

Seismically-induced displacements increase as a result of lower internal shear strength, as shown in Fig. 9a. However, it is not clear to what degree the observed amplification for blocks between deep tension cracks (Fig. 8d) also contributes to enhancing overall displacements. In the following experiment, we explore whether amplification related to tension cracks modifies the wavefield such that dislocation along the sliding surface is enhanced, or if it is merely a localized effect that has little impact on the global response. We performed a simplified experiment in which two deep tension cracks, separated by 50 m, were inserted in the elastic sliding block (Fig. 10). Although the tension cracks can open to a prescribed depth, the sliding block may only deform elastically. The depths of the two tension cracks were varied from 50 to 200 m.

Fig. 10b shows the amplification pattern at the ground surface for a model with two 150 m deep tension cracks. Amplification of up to a factor 7 occurs at 3.3 Hz. In contrast, amplification along the sliding surface is consistently less than 2 (Fig. 10c), and there is no amplification maximum below the tension cracks corresponding to that at the ground

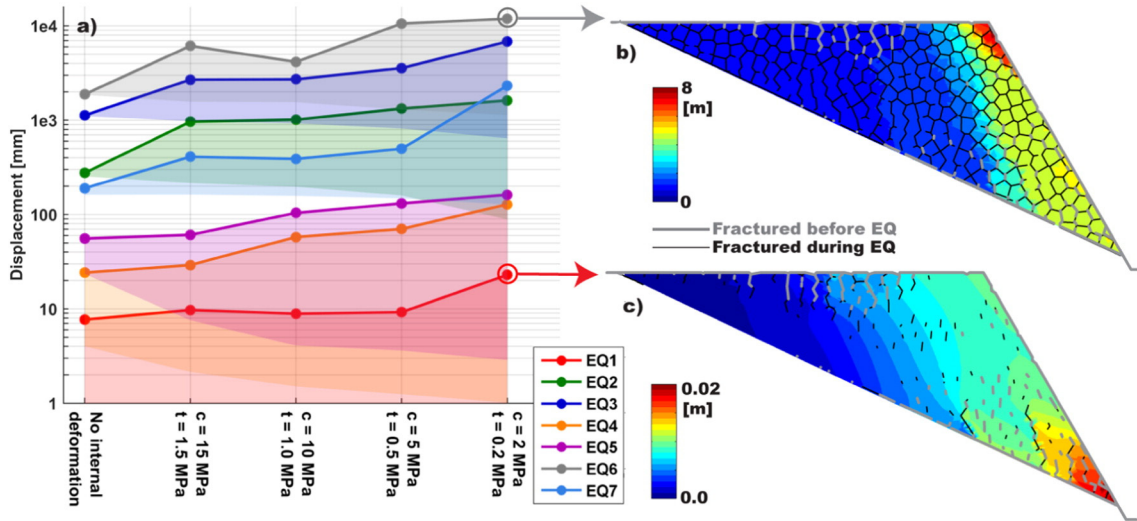


Fig. 9. a) Displacements induced by seven ground motions (Fig. 2) as a function of discontinuity strength. Thick line represents the maximum displacement while shading shows the range between minimum and maximum displacements. b) and c) show the displacement field induced by two different ground motions, EQ6 and EQ1, respectively. Gray lines represent fractures that failed prior to the earthquake under gravity alone, while black lines indicate fractures that failed in response to the earthquake.

surface. The presence of tension cracks does not considerably alter amplification characteristics along the sliding plane. We conclude that large localized amplification (factors of up to 10) on individual blocks within the instability likely plays only a minor role in enhancing overall co-seismic slope displacements. Such amplification patterns are, however, indicators of critical stresses and internal fracturing within a rock mass, which suggest low static factor of safety conditions. Fig. 10d

shows spectral amplifications computed for different tension crack depths at two points: one located along the slope crest and another located between the two tension cracks (see dots in Fig. 10a). Amplification at the topographic frequency f_T (i.e. the first amplification maximum on the slope crest) increases only slightly from 1.4 to 1.7 with increasing tension crack depth, while f_T itself remains constant. Between the two tension cracks, strong amplification peaks appear

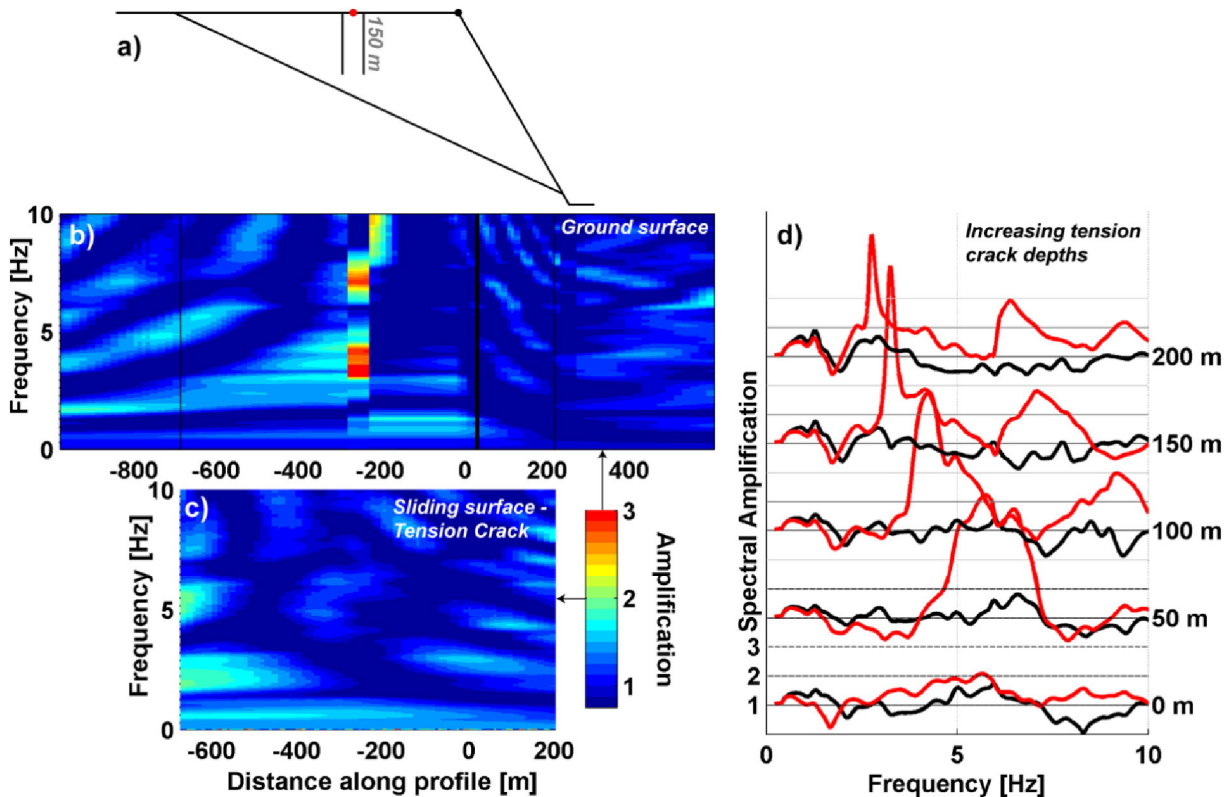


Fig. 10. a) Geometry used to explore the role of tension cracks on seismic slope response. Tension cracks reach depths of 50, 100, 150 m, and 200 m. The 200 m tension crack intersects the sliding surface. b) Amplification at the ground surface for tension fractures reaching 150 m. c) Corresponding amplification along the sliding surface. d) Spectral amplification at the slope crest (black line) and on the block separated by tension fractures (red line) for different fracture depths. (For interpretation of the references to color in this figure legend, the reader is referred to the web version of this article.)

reaching factors of 5 to 7. These occur at frequencies of 5.7, 4.3, 3.3 and 2.8 Hz for tension crack depths of 50, 100, 150 and 200 m, respectively. There is a systematic change of amplification frequency with tension crack depth, which implies that block dimensions may be inferred from amplification frequencies using numerical modeling.

5.3. Repeated seismic loading

In real cases of slope instability, internal strength degradation may result from progressive weakening, for example by repeat earthquakes. The importance of seismic pre-conditioning has been hypothesized for many earthquake-triggered landslides. Moore et al. (2012) describes the case of the 1946 Rawilhorn rock avalanche in Switzerland, which was triggered by a M_w 6.0 aftershock following the M_w 6.1 main shock (Fritsche and Fäh, 2009). They hypothesized that the first earthquake weakened the rock mass, leaving it in a critical state susceptible for triggering during the second event. A further example of seismic pre-conditioning may be the 2008 Wenchuan earthquake. Parker (2013) lists earthquakes with substantial numbers of triggered landslides during the past 25 years. The 2008 Wenchuan earthquake stands out due to the exceptional number of landslides triggered; a history of repeated earthquake-induced damage may have left many of the slopes highly susceptible to failure during the earthquake. We investigate the impact of progressive strength degradation on the seismic response of deep-seated slope instabilities by exposing the slope shown in Fig. 8b (i.e. 10 MPa cohesion) to a sequence of up to four earthquakes. The case corresponds to a slope in which a strong and undisturbed rock mass experiences first-time damage followed by progressive damage accumulation (similar to Lenti and Martino, 2012).

5.3.1. Amplification

Fracture networks following each earthquake are shown in Fig. 11, along with corresponding amplification patterns. Similar to the results in Fig. 8, strong localized spectral amplifications are associated with newly-formed deep tension cracks behind the slope crest. Note that only little additional fracturing occurs between the second and third earthquakes (Fig. 11b and c), but amplification at 3.5 Hz in the area of the tension cracks increases from a factor 11 to 14. After the fourth earthquake, this peak has reduced to a factor 8, while a complex pattern of large amplifications at higher frequencies appears as a consequence of intense fracturing (Fig. 11d). Spectral amplifications at the slope crest are less strongly affected, and only increase from ~1.5 to ~2.5. Here the localized amplification patterns arise only from the compliant response of fractures that opened due to intense deformation. In a more realistic rock mass, strong deformation and fracturing as shown in Fig. 11d would also degrade the rock mass stiffness, resulting in additional amplification related to material contrasts (as in Fig. 6). A transition from fracture- to material-contrast related amplification would occur, as well as a combination of the two effects. Our results show that amplification characteristics are extremely sensitive to changes in the fracture network within a rock mass. However, the effects are not systematic. Changes are observed in both the frequency and amplification factors, and as a consequence, interpretation of amplification patterns towards structural properties of the rock mass (block sizes, fracture depths, etc.) is challenging.

5.3.2. Displacements

Fig. 12 shows displacements induced by the earthquake ground motions from Fig. 2 for multiple events; the impact of seismic pre-conditioning is dramatic. Displacements can be more than an order of magnitude larger when the slope has already experienced damage from a previous earthquake, as compared to when no previous earthquake damage has occurred. Note that many of the models are only run for a maximum of 40 s (which includes the entire earthquake time history). However, displacements often exceed 10–100 m (EQ2, EQ3, EQ6), which implies the onset of catastrophic failure.

These results illustrate the role of repeated seismic loading as a long-term fatigue process that contributes to progressive failure of a relatively competent stable rock slope (recall fracture cohesion is 10 MPa), and hence is highly efficient for deforming and damaging rock slope instabilities. We also observe that co-seismic displacement strongly depends on pre-existing damage, and thus on the inherited cumulative effects of a landslide's seismic exposure. Substantial pre-existing damage is in turn revealed by strong and localized amplification patterns (Fig. 11, Burjáněk et al., 2010, 2012; Moore et al., 2011). The phenomenon is further explored by Gischig et al. (in review).

6. Comparison to Newmark-type methods

We compare displacements computed in UDEC (for 25 and 425 m high slopes) with widely-used Newmark-type sliding block methods (see Jibson, 2011, or Newmark, 1965 for a detailed description of the method). Sliding block displacements were computed using SLAMMER (Jibson et al., 2013), in which a variety of Newmark-type methods are implemented. They range from the simplest approach, the original rigid-block method of Newmark (1965), to the more sophisticated, coupled sliding block method of Rathje and Bray (1999), which also considers the height and seismic velocity of the sliding body. A total of 150 ground motions were used for comparison, and the resulting displacements are shown in Fig. 13. These represent maximum displacements for the sliding block, while the range between minimum and maximum displacements is indicated by gray lines below each data point. The color code corresponds to the mean frequency of each ground motion record (scale in Fig. 13h).

The comparisons were first performed for homogeneous slopes. UDEC results for the 25 m high slope show consistently larger predicted displacements than the rigid-block Newmark approach (Fig. 13a). The difference is usually less than a factor of two, but can reach up to factors of 10 for small displacements. UDEC often predicts displacements of several millimeters for input motions that produce no displacements in the rigid-block method. Results do not change dramatically for the coupled Newmark analysis (Fig. 13b). Although displacements group more closely to the line of equality (i.e. where both methods give equal results), the largest differences are similar as for the rigid-block analysis. One reason explaining deviations between UDEC and the rigid-block method is the difference in how ground motions are applied. In the rigid-block method, ground motions are applied tangentially to the sliding plane (see Fig. 3 in Jibson, 2011), and thus only the tangential acceleration varies. In UDEC, ground motion is applied at the bottom of the model, and variations of both the tangential and normal components of stress occur as the shear wave propagates upward. Simple scoping calculations (not presented here) show that Newmark displacements tend to increase if both the tangential and normal components are considered.

Nevertheless, differences up to an order of magnitude only occur for UDEC displacements smaller than 10 mm. For a slope of this large size, such displacements are usually considered insignificant for global stability. As Jibson (2011) emphasizes, displacements from Newmark methods must be interpreted cautiously, i.e., they merely serve as an index of landslide susceptibility and do not represent actual estimates of co-seismic displacement. To explore deviations between predicted UDEC and Newmark displacements in a hazard assessment context, we grouped the displacements presented in Fig. 13a and b into different classes: 0–1 cm, 1–10 cm, 10 cm–1 m, and >1 m (Fig. 13c). Displacements predicted in UDEC are slightly fewer in number in the smallest class, and marginally more frequent in the two largest classes. Generally, the three methods produce comparable results.

For the 425 m slope, differences between UDEC and Newmark results are greater (Fig. 13d and e). Differences are again most pronounced at smaller displacements, and for rigid-block displacements of zero to a few millimeters, UDEC may predict several centimeters. Differences also depend on the mean frequency (f_m) of ground motion: the

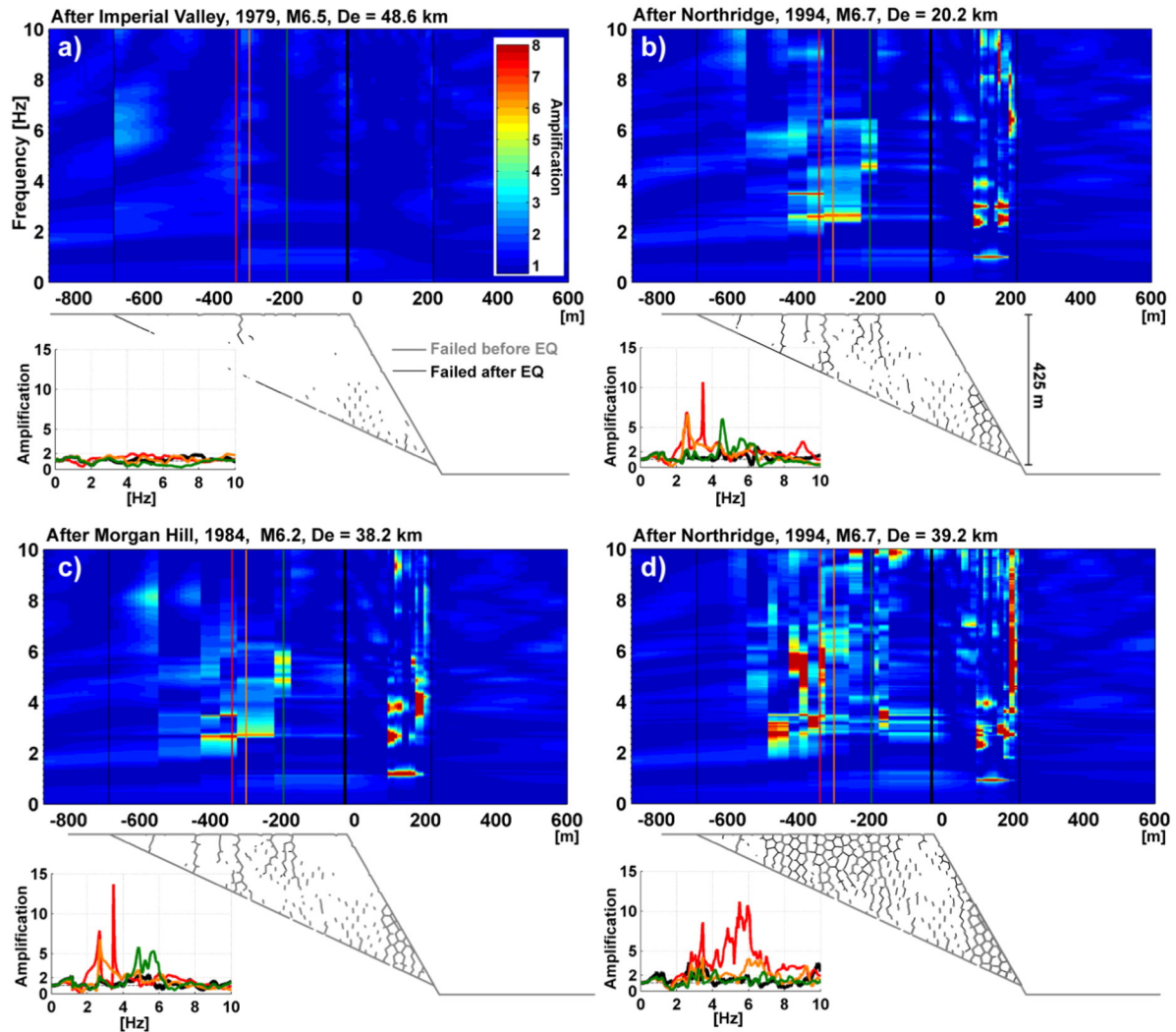


Fig. 11. Results of models incorporating internal fracturing (Fig. 8b, $c = 10$ MPa, $t = 1$ MPa), and shaken by a sequence of (a) one to (d) four earthquakes. Conditions after each model run serve as the starting model for the next earthquake. Hence, in (a) the slope has been damaged by one earthquake, (b) by two earthquakes, and so on. Similar to Fig. 8, amplification patterns at the ground surface are shown on top, while failed discontinuities after each earthquake are shown below. Gray fractures are those that failed during the previous earthquake (and due to gravity-driven displacements), black fractures have failed during the current earthquake. Spectral amplification at the slope crest and at different blocks separated by tension cracks (see colored lines) is also shown. (For interpretation of the references to color in this figure legend, the reader is referred to the web version of this article.)

ratio between UDEC and rigid-block displacements increases at lower f_m . In contrast, predicted UDEC displacements smaller than the rigid-block displacements usually occur at high f_m . Similar results were found by Lenti and Martino (2012), who noted both over- and under-prediction by sliding block analysis depending on slope height and angle. However, this f_m -dependence vanishes in the coupled analysis (Fig. 13e). Differences also become smaller at larger displacements. However, at small displacements, differences between UDEC and Newmark results can still be more than an order of magnitude. Nevertheless, the improvement achieved by the coupled analysis relative to the rigid-block approach emphasizes the importance of accounting for the ground motion frequency content in relation to slope height. The closer f_m is to 0.5 to 1 Hz, the larger the deviations of the rigid-block method; i.e. ground motions that include dominant wavelengths larger than 5 to 10 times the slope height produce larger deviations. Coupled Newmark analysis partly accounts for this.

Fig. 13f shows that the strongest deviations between UDEC and Newmark results occur at small displacements. Fewer UDEC displacements fall in the <1 cm group, rather shifting to the 1–10 cm category. In the two groups representing the largest displacements (10 cm–1 m,

and <1 m), the results are similar. For the 425 m homogeneous slope, differences at small displacements can be more than an order of magnitude, while at larger displacements – those more relevant for slopes of this scale – Newmark methods perform reasonably well.

In Fig. 13g and h, we compare predicted displacements for models with and without velocity contrasts for the seven ground motions in Fig. 2, with the goal of exploring whether the presence of a velocity contrast is sufficiently accounted for by the coupled Newmark analysis. Large differences with factors of 2 to 5, arising from a velocity contrast of 3, are not reduced using the coupled analysis. Hence, the existence of velocity contrasts can be a source of significant underestimation of displacements using Newmark-type methods.

Comparisons between displacements predicted in UDEC when internal fracturing is allowed (cohesion = 2 MPa) and the two Newmark methods are shown in Fig. 13i and j. UDEC displacements can reach up to two orders of magnitude higher, however, the range of displacements within the slope spans at least one order of magnitude. Nearly no UDEC displacements fall into the <1 cm category in Fig. 14k, while they dominate in the other three groups. The most striking difference is for the >1 m group, which contains more than 30% of UDEC

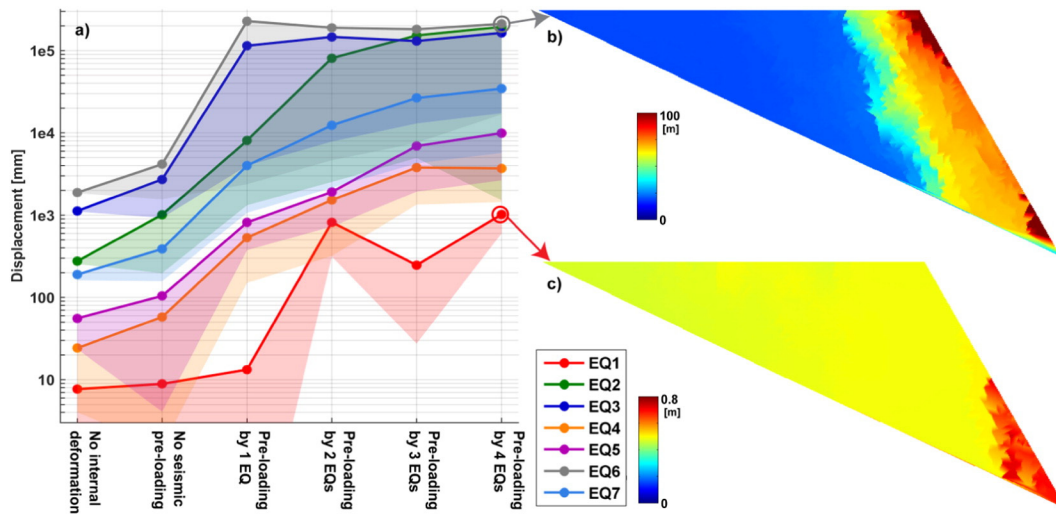


Fig. 12. a) Computed displacements (maximum and minimum) resulting from seven ground motions (Fig. 2) as a function of earthquake-induced damage prior to each ground motion. For comparison we also show the case with no earthquake damage (corresponding to Fig. 8b) and the case of a sliding block where internal fracturing was not allowed (Fig. 3b). b) and c) Displacement field induced by EQ6 and EQ1, respectively. Note that models were stopped after 40 s, after the earthquake. However, block displacements did not stop in these cases, as they had not reached a new mechanical equilibrium, meaning the slope is in the process of failing catastrophically.

displacements but only a few percent from the Newmark results. Hence, in cases where strong internal fracturing is expected, Newmark-type displacements may severely under-predict seismic landslide hazard.

7. Discussion

7.1. Conditions favoring co-seismic slope deformation

We investigated three groups of amplification phenomena affecting large, deep-seated rock slope instabilities – geometry, material contrasts, and internal fracturing – and examined their roles in enhancing seismically-induced slope deformation. These are illustrated in Fig. 14, along with key results regarding amplification factors and increasing displacements from our sensitivity study. As long as the rock mass forming the slope is homogeneous and does not deform internally, slope height and topography have little net effect on amplification and slope displacement. A slope with minimal topography (i.e. flat surface behind the slope crest) can experience amplification factors of up to 1.5. Increasing slope height can lead to larger (up to 2) or smaller (~ 0.25) displacement factors depending on ground motion characteristics. Similar relationships between slope height and co-seismic displacement were found by Bouckovalas and Papadimitriou (2005) and Lenti and Martino (2012). Extreme slope relief can enhance amplification by up to a factor of 2.5. The impact on displacement however is relatively small; displacements increase by factors ranging from 1.1 to 1.6. In comparison, the presence of a material contrast has a larger impact. Waves reflected at the surface and at velocity interfaces produce constructive interference. As a consequence, amplification factors reach 7 and displacements increase by a factor of 5.3 (but can also vary between 1 and 2), when the seismic velocity contrast is 3. Note that velocity contrasts in nature may be even larger than 3 and thus result in even stronger amplification. Bourdeau and Havenith (2008) computed amplification factors of 15 for a three layer model with contrast between the highest (bedrock) and lowest (surficial soil) seismic velocity of >6 . Strong contrasts in material properties can result from either lithological changes (e.g. soil–bedrock interface as explored by Bourdeau and Havenith, 2008), or from a long deformation history that has led to intense fracturing and reduced material stiffness compared to the stable bedrock (e.g. Bonzanigo et al., 2007). We found that the most pronounced site effects occur in slopes with internal plastic deformation. Deep, open tension cracks resulting from degraded material strength create localized amplification maxima with factors >10 at distinct frequencies characteristic of the blocks delineated by cracks.

Similarly, degraded internal strength allows mobilization of individual blocks within the landslide body. Thus, displacements can increase by more than one order of magnitude at lower strengths. Internal strength can in turn be degraded as a consequence of preceding earthquakes (see also Gischig et al., in review), or other progressive failure mechanisms such as seasonal precipitation (Smithyman et al., 2009; Preisig et al., in review) or thermal cycles (Gischig et al., 2011b). Our results are in agreement with Burjáněk et al. (2014), who found that amplification factors larger than 2 observed in locations with pronounced topography were more likely related to the local shear wave velocity structure than geometric effects.

Fig. 14 also illustrates that multiple factors favoring enhanced co-seismic displacements may occur concurrently, thus resulting in an even stronger instability response to earthquakes. In a realistic complex, deep-seated landslide (as opposed to our strongly simplified slope configuration), we expect that all factors may contribute to the seismic response to some degree. Such large landslide bodies typically contain straight, curved or composite sliding surfaces with varying kinematics, and may involve entire valley flanks in areas of high relief. They may also consist of several rock types with different material properties. Often they have experienced a history of substantial progressive damage and deformation resulting in reduced material stiffness (i.e. strong material contrasts), and strength degradation (promoting internal deformation). In particular, internal deformation is likely to occur due to the presence of discontinuities, differential displacements, and extensional strains. In contrast, sliding as a single rigid-block is less realistic, except for small volume slope instabilities where a sliding surface coincides with intersecting persistent discontinuities (e.g., wedge failure). Hence, in most adverse but also realistic situations, strong relief, coupled with seismic velocity contrasts, may enhance the seismic response of a deep-seated slope instability, while internal fracturing must be anticipated as an important mechanism aiding additional (and time-dependent) development of earthquake-triggered landslides. Further effects of 3D geometry are expected in realistic landslide cases. We argue that 3D effects would enhance geometric amplification. However, for material contrasts or internal fractures, we cannot infer implications of 3D effects from our 2D analysis. This should be addressed in future studies.

In this light, we consider the results of simplified methods (i.e. Newmark-type approaches) for seismic slope stability analysis to be overly optimistic for hazard assessment of deep-seated slope instabilities. Note that regression models derived from Newmark's analysis by

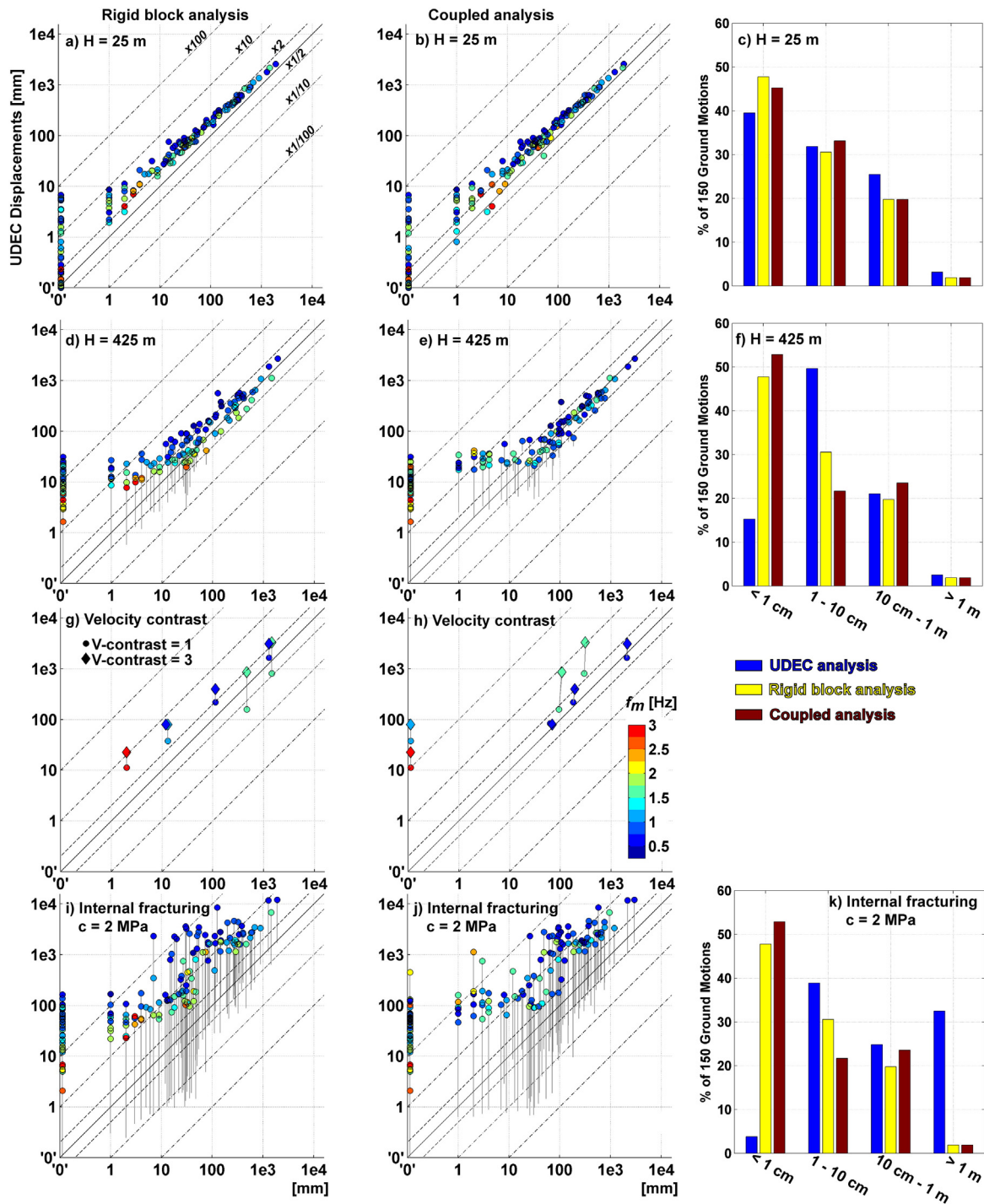


Fig. 13. Comparison of UDEC displacements with Newmark-type methods (i.e. rigid block and coupled analysis). a) and b) Results for the 25 m high slope and 150 ground motions. Color code represents mean frequency, f_m of each ground motion. c) Number of cases falling in displacement bins of > 1 cm, 1–10 cm, 10 cm–1 m, and > 1 m. d), e) and f) Results for a 425 m slope. g) and h) Comparison of results for cases with seismic velocity contrast of 1 and 3 for the seven ground motions in Fig. 2. i) and j), and k) Results with internal fracturing allowed (case in Fig. 8d). (For interpretation of the references to color in this figure legend, the reader is referred to the web version of this article.)

various authors (e.g. Jibson, 2007; Bray and Travararou, 2007) anticipate a large scatter of displacements with standard deviations corresponding to a factor of 4.5. Hence, the variation of displacement with varying slope height or topography determined in our study is well within this margin of error. If displacements are treated simply as an index of seismic landslide hazard (Jibson, 2011), then slope height or topographic effects alone do not justify the use of more complex numerical models (Fig. 13c and f). Moreover, the coupled method proposed

by Rathje and Bray (1999) can account for the effect of slope height (Fig. 13e). However, as internal fracturing is likely for large landslides, Newmark-type methods significantly underestimate induced slope displacements. More realistic assessments of the seismic response of large landslides require detailed numerical analysis. The advantage of numerical methods is that they are not only capable of predicting slope displacement fields more realistically, but if rock mass behavior and properties are well constrained, the model may also provide estimates

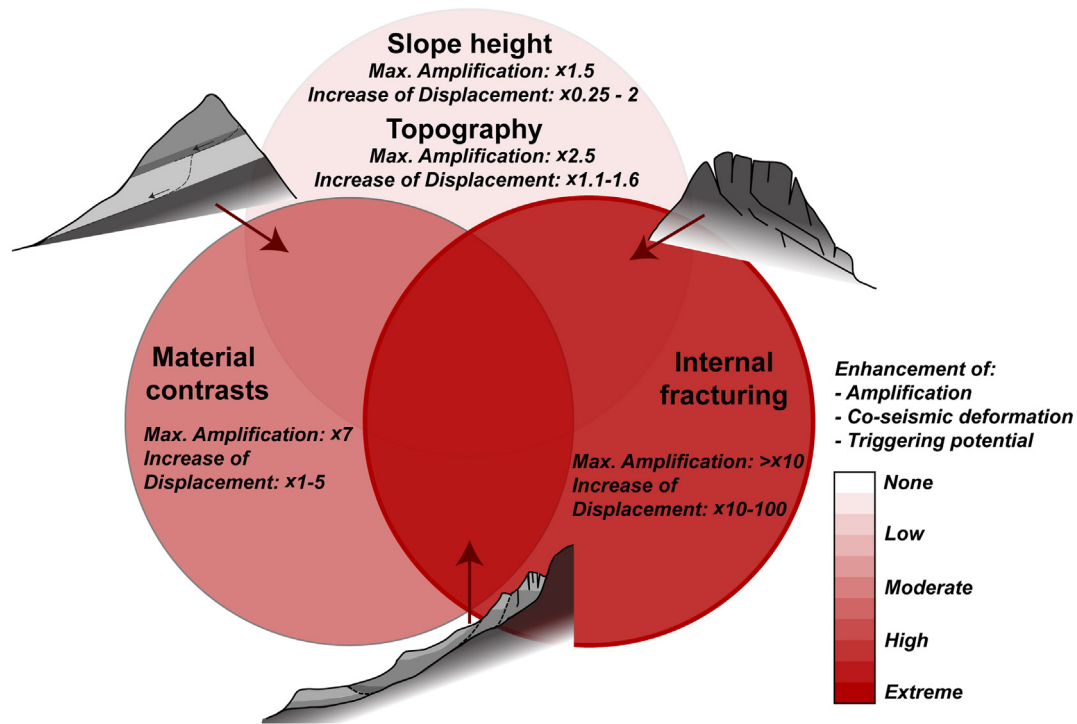


Fig. 14. Summary of amplification factors and enhanced co-seismic displacement resulting from three types of amplification: 1) geometric amplification (slope height, topography), 2) amplification due to material contrasts, and 3) amplification due to internal fracturing (compliant fractures). Sketches depict situations where two amplification phenomena may occur at the same time. Both amplification and enhanced displacement may be stronger if two or three amplification phenomena act simultaneously. The occurrence of internal fracturing – the cause of strong localized amplification and enhanced co-seismic deformation – is commonly encountered in large, deep-seated slope instabilities.

of critical displacement values above which catastrophic failure is inevitable. Numerical investigations towards such critical displacements will be the subject of future research.

7.2. Impact of ground motion characteristics

Ground motions explored here to study the variation of seismic response with slope height did not reveal any singular trend (Fig. 4). Increasing slope height can result in larger, smaller or equal displacements in different earthquakes. Similarly, variation of displacement with topography and seismic velocity contrasts do not exhibit simple patterns (Figs. 5b and 7). Displacements may remain nearly constant regardless of seismic velocity contrasts (EQ5, Fig. 7) or increase by a factor of 5 (EQ2). Ground motion characteristics, such as frequency content, determine the variable response for different slope conditions, although in a complex manner. Past studies have recognized that ground motion frequency content must be considered in seismic slope stability analyses. Bray et al. (1998), for example, included the mean period T_m and duration of strong ground motion in their seismic design procedure. In this study, we also compared mean frequency f_m and frequency f_{PSA} at the peak of the acceleration spectrum with modeled amplification patterns to explore the different displacement versus slope-height trends. However, no systematic relationship explaining increasing or decreasing trends could be identified (Fig. 4b–e). Only for some ground motions did we observe trends between amplification at frequency f_m or f_{PSA} along the sliding surface that explain some of the displacement patterns (Fig. 4d and e). The interaction of seismic waves with the slope cannot be understood by comparing a single metric such as f_m or f_{PSA} with slope-specific amplification patterns, because wave–slope interaction is more spatially and temporally complex.

Nevertheless, we did observe a relationship between induced displacements and the proximity of f_m to frequencies corresponding to wavelengths 4 to 8 times the slope height. In the case of a 425 m high

slope, these wavelengths correspond to frequencies of 1.3 Hz (4 times slope height) and 0.65 Hz (8 times slope height). Fig. 13d shows that displacements are enhanced by more than a factor of 2 for ground motions with predominant frequencies at or below this range, as compared to the rigid block solution. The importance of low frequency energy was also observed by Bray and Travarasou (2007). They found that spectral acceleration at the period $1.5T_s$, where $T_s = 4H/V_s$, can explain part of the scatter in displacements predicted by coupled Newmark analyses, and included this in their regression model for co-seismic displacements. A characteristic of low frequency seismic waves is that they are large enough to produce deformations that involve the entire sliding body simultaneously, and thus are particularly efficient at inducing displacements. These waves are amplified by a factor of two along a major portion of the sliding surface (Fig. 3c and d), a result of the free surface effect penetrating to depths larger than the slope height. Shorter wavelengths do not simultaneously deform the entire sliding body. The same wave may act to promote slip along one portion of the sliding surface and, at the same time, inhibit slip along another portion. Amplification of such waves is also spatially heterogeneous (Fig. 3c and d). Hence, the seismic response to wavelengths smaller than about four times the slope height is less predictable. We conclude that for co-seismic displacement it is most relevant whether a wave is able to deform the unstable rock mass as a whole. In the case of shorter wavelengths, the strain field is more heterogeneous in the rock mass, and thus it is important how they interact with critically-stressed discontinuities or intact rock bridges in different regions of the slope at different times. The complexity of wave–slope interactions uncovered here also implies that seismic slope stability models should not rely on a single input ground motion that might be characteristic of an expected earthquake at a given site, or on simplified waveforms such as sinusoids. Ground motions of two earthquakes with similar magnitude and depth, recorded at similar distance, may have significantly different waveforms and frequency content. Note that EQ2 and EQ6 were recorded at about the

same epicentral distance (Fig. 2), but EQ2 is from a M7.6 earthquake, while EQ6 is from a M6.7 earthquake. It is surprising that the M6.7 earthquake produces larger displacements than the M7.6 earthquake (Fig. 5). However, we acknowledge that the M6.7 ground motion is affected by local site effects, and exhibits lower mean frequency ($f_m = 1.4$) compared to the M7.6 ($f_m = 4.1$); i.e. wavelengths of the smaller earthquake are able to excite the entire sliding mass, which is not the case for the larger earthquake. Although EQ6 may not necessarily be a realistic input ground motion for a deep-seated landslide (because it was recorded on soil and thus contains site-specific effects), the example nevertheless illustrates that seismic slope stability analyses must be performed using a considerable range of realistic ground motions in order to anticipate complexity in the potential seismic slope response.

7.3. Implications of amplification characteristics

The relevance of site amplification in seismic slope stability assessment is widely acknowledged (e.g., Del Gaudio and Wasowski, 2011; Bourdeau and Havenith, 2008). Our study demonstrates, however, that it is not trivial to include observations of amplification in co-seismic landslide hazard analyses. As discussed above, the fundamental frequency of a slope cannot be extracted directly from amplification patterns. Amplification related to excitation of resonant frequencies is partly concealed by wave focussing and interference (Ashford et al., 1997; Geli et al., 1988). Additionally, amplification along the sliding surface, where co-seismic deformation actually induces damage, cannot seemingly be inferred from observable amplification patterns at the ground surface.

Although amplification patterns do not readily explain the variability in modeled co-seismic displacements, we point out that strong amplification is an indicator of potentially large seismic deformation. Amplification related to velocity contrasts and the presence of deep, open tension cracks is associated with larger displacements, as well as the most severe underestimates of displacements by Newmark-type methods. However, the mechanics of why displacements are enhanced may be different for each mechanism. Seismic velocity contrasts result in wave trapping within the sliding body, and co-seismic deformation along the sliding surface is more intense than in cases without velocity contrasts (Fig. 6). On the other hand, localized amplification due to open fractures does not considerably modify the wavefield at distances far from the open fractures (Fig. 10c). While such localized amplification affects the rock mass only locally, and may thus have little impact on global co-seismic deformation, it can importantly reveal the presence of deep tension cracks and associated degradation of rock mass strength. We resolve that the relevance of these amplification phenomena in site-specific assessment of seismic slope stability is indirect, because both are a reflection of internal deformation and material characteristics prior to earthquake shaking. Although direct use of amplification measurements in improving estimates of co-seismic displacements is not straightforward, its application is twofold: 1) it allows identification of slopes with reduced internal strength that may be more susceptible to earthquake-triggered failure, and 2) it serves as an important constraint for numerical models when performing detailed seismic stability analysis. Exploiting both these advantages relies on direct field observations of the local amplification characteristics (Burjánek et al., 2010, 2012, 2014; Del Gaudio et al., 2014; Danneels et al., 2008).

8. Conclusions

Our sensitivity analyses provide new insights into the causes and relationships between rock slope amplification phenomena and co-seismic displacement of deep-seated instabilities. We acknowledge that our slope models are strongly simplified and limited to 2D, and do not appropriately account for all complexity typically expected in deep-seated landslides. However, these simplifications were chosen to

allow extricating and distinguishing effects of different phenomena that contribute to the seismic response of a realistic deep-seated landslide (i.e. slope geometry and scale, material contrasts, and structures accommodating internal deformation). Application of the methodology developed here to a real case history is the subject of further research (see Wolter et al., in review).

From our sensitivity study we conclude that the strongest spectral amplifications were related to material contrasts and the presence of compliant large-scale discontinuities (such as open tension cracks), which in turn generated the largest displacements. In the case of seismic velocity contrasts, wave trapping within the landslide body resulted in greater slip. For compliant discontinuities, amplification related to open tension cracks may be diagnostic of degraded strength within the landslide body, as well as considerable accrued deformations prior to an earthquake. In this case, additional internal fracturing during subsequent earthquakes is expected, which in turn generates greater displacements. Large deep-seated rock slope instabilities are commonly populated by a considerable number of discontinuities. Hence, internal fracturing is likely and must be anticipated in seismic landslide hazard assessment. The use of simplified Newmark-type methods is inappropriate in this case, as they may severely underestimate co-seismic displacements. The effort of detailed numerical analysis is justified when the consequences of large deformation or catastrophic failure pose considerable risk.

Our study also shows that a straightforward link between spectral amplification and co-seismic displacements cannot be readily established. Although large amplification due to material contrasts or compliant discontinuities is associated with greater displacements, a certain amplification factor at a certain frequency characteristic of a particular ground motion cannot be translated into a simple estimate of displacements during an earthquake. However, measurements of the seismic response of an instability, such as amplification patterns and wave polarization characteristics derived from ambient noise surveys (Burjánek et al., 2010, 2012, 2014; Del Gaudio et al., 2014), or information from seismic velocity imaging (Heincke et al., 2006, 2010) can be interpreted to reveal material contrasts and internal structure within an unstable rock mass. Thus, such observations are useful to constrain geological and numerical models used for seismic slope stability analysis. The interaction of seismic waves and deep-seated instabilities is diverse in response to different ground motions, even when earthquake source characteristics are comparable. To anticipate the range of possible slope responses, seismic stability analyses must be performed using a representative suite of possible ground motions, which may be either real (e.g. SLAMMER, Jibson et al., 2013, or other databases) or synthetic (Allstadt et al., 2013).

Acknowledgments

This study was jointly funded by the Swiss National Science Foundation, project P300P2_151291, and a National Science and Engineering Research Council of Canada (NSERC) Accelerator Grant to O. Hungr. Constructive comments from Jan Burjánek and three anonymous reviewers substantially helped improve this manuscript.

References

- Allstadt, K., Vidale, J.E., Frankel, A.D., 2013. A scenario study of seismically induced landsliding in Seattle using broadband synthetic seismograms. *Bull. Seismol. Soc. Am.* 103, 6. <http://dx.doi.org/10.1785/0120130051>.
- Ashford, S.A., Sitar, N., Lysmer, J., Deng, N., 1997. Topographic effects on the seismic response of steep slopes. *Bull. Seismol. Soc. Am.* 87, 701–709.
- Bhasin, R., Kaynia, A.M., 2004. Static and dynamic simulation of a 700-m high rock slope in western Norway. *Eng. Geol.* 71, 213–226.
- Bonzanigo, L., Eberhardt, E., Loew, S., 2007. Long-term investigation of a deep-seated creeping landslide in crystalline rock. Part I. Geological and hydromechanical factors controlling the Campo Vallemaggia landslide. *Can. Geotech. J.* 44 (10), 1157–1180.
- Bouckovalas, G.D., Papadimitriou, A.G., 2005. Numerical evaluation of slope topography effects on seismic ground motion. *Soil Dyn. Earthq. Eng.* 25, 547–558.
- Bourdeau, C., Havenith, H.-B., 2008. Site effects modelling applied to the slope affected by the Suusamyr earthquake (Kyrgyzstan, 1992). *Eng. Geol.* 97, 126–145.

- Bozzano, F., Lenti, L., Martino, S., Paciello, A., Scarascia Mugnozza, G., 2008. Self-excitation process due to local seismic amplification responsible for the reactivation of the Salcito landslide (Italy) on 31 October 2002. *J. Geophys. Res.* 113, B10312. <http://dx.doi.org/10.1029/2007JB005309>.
- Bozzano, F., Lenti, L., Martino, S., Montagna, A., Paciello, A., 2011. Earthquake triggering of landslides in highly jointed rock masses: reconstruction of the 1783 Scilla rock avalanche (Italy). *Geomorphology* 129, 294–308.
- Bray, J.D., 2007. Simplified seismic slope displacement procedures. In: Pitalakis, K.D. (Ed.), *Earthquake Geotechnical Engineering*. Springer, pp. 327–353.
- Bray, J.D., Rathje, E.M., 1998. Earthquake-induced displacements of solid-waste landfills. *J. Geotech. Geoenviron.* 124, 242–253.
- Bray, J.D., Travasarou, T., 2007. Simplified procedure for estimating earthquake-induced deviatoric slope displacements. *J. Geotech. Geoenviron.* 133, 381–392.
- Bray, J.D., Rathje, E.M., Augello, A.J., Merry, S.M., 1998. Simplified seismic design procedures for geosynthetic-lined, solid waste landfills. *Geosynth. Int.* 5 (1–2), 203–235.
- Burjānek, J., Gassner-Stamm, G., Poggi, V., Moore, J.R., Fäh, D., 2010. Ambient vibration analysis of an unstable mountain slope. *Geophys. J. Int.* 180 (2), 820–828. <http://dx.doi.org/10.1111/j.1365-246X.2009.04451.x>.
- Burjānek, J., Moore, J.R., Molina, F.X.Y., Faeh, D., 2012. Instrumental evidence of normal mode rock slope vibration. *Geophys. J. Int.* 188, 559–589.
- Burjānek, J., Edwards, B., Faeh, D., 2014. Empirical evidence of local seismic effects at sites with pronounced topography: a systematic approach. *Geophys. J. Int.* <http://dx.doi.org/10.1093/gji/ggu014>.
- Chigira, M., Wang, W.-N., Furuya, T., Kamai, T., 2003. Geological causes and geomorphological precursors of the Tsaoling landslide triggered by the 1999 Chi-Chi Earthquake, Taiwan. *Eng. Geol.* 68, 259–273.
- Crosta, G.B., Imposimato, T.S., Roddeman, D., Chiesa, S., Moia, F., 2005. Small fast-moving flow-like landslides in volcanic deposits: the 2001 Las Colinas Landslide (El Salvador). *Eng. Geol.* 79, 185–214.
- Cui, P., Zhu, Y.Y., Han, Y.S., Chen, X.Q., Zhuang, J.Q., 2009. The 12 May Wenchuan earthquake-induced landslide lakes: distribution and preliminary risk evaluation. *Landslides* 6, 209–223.
- Cundall, P.A., Hart, R.D., 1992. Numerical modelling of discontinua. *Eng. Comput.* 9, 101–113.
- Danneels, G., Bourdeau, C., Torgoev, I., Havenith, H.-B., 2008. Geophysical investigation and dynamic modelling of unstable slopes: case-study of Kainama (Kyrgyzstan). *Geophys. J. Int.* 175, 17–34. <http://dx.doi.org/10.1111/j.1365-246X.2008.03873.x>.
- Del Gaudio, V., Wasowski, J., 2011. Advances and problems in understanding the seismic response of potentially unstable slopes. *Eng. Geol.* 122, 73–83. <http://dx.doi.org/10.1016/j.enggeo.2010.9.007>.
- Del Gaudio, V., Muscillo, S., Wasowski, J., 2014. What we can learn about slope response to earthquakes from ambient noise analysis: an overview. *Eng. Geol.* <http://dx.doi.org/10.1016/j.enggeo.2014.05.010>.
- Dunning, S.A., Mitchell, W.A., Rosser, N.J., Petley, D.N., 2007. The Hattian Bala rock avalanche and associated landslides triggered by the Kashmir earthquake of 8 October 2005. *Eng. Geol.* 93, 130–144.
- Evans, S.G., Bent, A.L., 2004. The Las Colinas landslide, Santa Tecla: a highly destructive flowslide triggered by the January 13, 2001, El Salvador earthquake. In: Rose, W.I., Bommer, J.J., Lopez, D.L., Carr, M.J., Major, J.J. (Eds.), *Natural Hazards in El Salvador*. Special Paper 375. Geological Society of America, Boulder, Co, pp. 25–38.
- Fritsche, S., Fäh, D., 2009. The 1946 magnitude 6.1 earthquake in the Valais: site-effects as contributor to the damage. *Swiss J. Geosci.* 102, 423–439.
- Geli, L., Bard, P.Y., Julien, B., 1988. The effect of topography on earthquake ground-motion: a review and new results. *Bull. Seismol. Soc. Am.* 78, 42–63.
- Gischig, V., Amann, F., Moore, J.R., Loew, S., Eisenbeiss, H., Stempfhuber, W., 2011a. Composite rock slope kinematics at the current Randa instability, Switzerland, based on remote sensing and numerical modeling. *Eng. Geol.* 118, 37–53.
- Gischig, V., Moore, J.R., Evans, K.F., Amann, F., Loew, S., 2011b. Thermo-mechanical forcing of deep rock slope deformation — part II: the Randa rock slope instability. *J. Geophys. Res.* B 116, F04011.
- Gischig, V., Preisig, G., Eberhardt, E., 2015w. Seismically-induced rock mass fatigue in deep-seated landslides. *Rock Mech. Rock Eng.* (in review).
- Hadley, J.B., 1964. Landslides and related phenomena accompanying the Hebgen Lake earthquake of August 17, 1959. *U. S. Geol. Surv. Prof. Pap.* 435-K, 107–138.
- Heincke, B., Maurer, H., Green, A., Willenberg, H., Spillmann, T., Burlini, L., 2006. Characterizing an unstable mountain slope using shallow 2D and 3D seismic tomography. *Geophysics* 71 (6), B241–B256. <http://dx.doi.org/10.1190/1.2338823>.
- Heincke, B., Günther, T., Dalsegg, E., Rønning, J.S., Ganerød, G.V., Elvebakk, H., 2010. Combined three-dimensional electric and seismic tomography study on the Åknes rockslide in western Norway. *J. Appl. Geophys.* 70, 292–306.
- Hoek, E., Diederichs, M.S., 2006. Empirical estimation of rock mass modulus. *Int. J. Rock Mech. Min. Sci.* 43, 203–215.
- Huang, R., Fan, X., 2013. The landslide story. *Nat. Geosci.* 6, 325–326.
- Huang, R., Pei, X., Fan, X., Zhang, W., Li, S., Li, B., 2012. The characteristics and failure mechanism of the largest landslide triggered by the Wenchuan earthquake, May 12, 2008, China. *Landslides* 9, 131–142. <http://dx.doi.org/10.1007/s10346-011-0276-6>.
- Itasca, 2011. UDEC — Universal Distinct Element Code, Version 5.0 User's Manual. Itasca Consulting Group, Inc., Minneapolis.
- Jibson, R.W., 2007. Regression models for estimating coseismic landslide displacement. *Eng. Geol.* 91, 209–218.
- Jibson, R.W., 2011. Methods for assessing the stability of slopes during earthquakes—a retrospective. *Eng. Geol.* 122, 43–50.
- Jibson, R.W., Harp, E.L., Michael, J.M., 2000. A method for producing digital probabilistic seismic landslide hazard maps. *Eng. Geol.* 58, 271–289.
- Jibson, R.W., Rathje, E.M., Jibson, M.W., Lee, Y.W., 2013. SLAMMER—Seismic Landslide Movement Modeled using Earthquake Records: U.S. Geological Survey Techniques and Methods. U.S. Geological Survey Techniques and Methods, Book 12 (chap. B1, unpagged).
- Kuhlemeyer, R.L., Lysmer, J., 1973. Finite element method accuracy for wave propagation problems. *J. Soil Mech. Found. Div. ASCE* 99, 421–427 (SM5).
- Lenti, L., Martino, S., 2012. The interaction of seismic waves with step-like slopes and its influence on landslide movements. *Eng. Geol.* 126, 19–36.
- Lenti, L., Martino, S., 2013. A parametric numerical study of the interaction between seismic waves and landslides for the evaluation of the susceptibility to seismically induced displacements. *Bull. Seismol. Soc. Am.* 103 (1), 33–56.
- Levy, C., Baillet, L., Jongmans, D., Mourou, P., Hantz, D., 2010. Dynamic response of the Chamouset rock column (Western Alps, France). *J. Geophys. Res.* 115, F04043.
- Moore, J.R., Gischig, V.S., Burjānek, J., Loew, S., Faeh, D., 2011. Site effects in unstable rock slopes: dynamic behavior of the Randa instability (Switzerland). *Bull. Seismol. Soc. Am.* 101 (6), 3110–3116.
- Moore, J.R., Gischig, V., Amann, F., Hunziker, M., Burjānek, J., 2012. Earthquake-triggered rock slope failures: damage and site effects. *Proceedings 11th International Symposium on Landslides*. CRC Press, Banff, Alberta, pp. 869–874.
- Newmark, N.M., 1965. Effects of earthquakes on dams and embankments. *Geotechnique* 15, 139–159.
- Owen, L.A., Kamp, U., Khattak, G.A., Harp, E., Keefer, D.K., Bauer, M., 2008. Landslides triggered by the October 8, 2005, Kashmir earthquake. *Geomorphology* 94, 1–9.
- Parker, R.N., 2013. Hillslope Memory and Spatial and Temporal Distributions of Earthquake-induced Landslides. (Durham theses), Durham University (Available at Durham E-Theses Online: <http://etheses.dur.ac.uk/7761/>).
- Plafker, G., Ericksen, G.E., 1978. Nevados Huascaran avalanches, Peru. In: Voight, B. (Ed.), *Rockslices and Avalanches*. Elsevier Scientific Press, New York, pp. 277–314.
- Preisig, G., Eberhardt, E., Smithyman, M., Preh, A., 2015w. Hydromechanical rock mass fatigue in deep-seated landslides accompanying the seasonal variations of pore pressures. *Rock Mech. Rock Eng.* (in review).
- Rathje, E.M., Bray, J.D., 1999. An examination of simplified earthquake-induced displacement procedures for earth structures. *Can. Geotech. J.* 36, 72–87.
- Sepúlveda, S.A., Murphy, W., Petley, D.N., 2005a. Topographic controls on coseismic rock slides during the 1999 Chi-Chi earthquake, Taiwan. *Q. J. Eng. Geol. Hydrogeol.* 38, 189–196. <http://dx.doi.org/10.1144/1470-9236/04-062>.
- Sepúlveda, S.A., Murphy, W., Jibson, R.W., Petley, D.N., 2005b. Seismically induced rock slope failures resulting from topographic amplification of strong ground motions: the case of Pacoima Canyon California. *Eng. Geol.* 80, 336–348.
- Sepúlveda, S., Serey, A., Lara, M., Pavez, A., Rebolledo, S., 2010. Landslides induced by the April 2007 Aysén Fjord earthquake, Chilean Patagonia. *Landslides* 7, 483–492.
- Smithyman, M., Eberhardt, E., Hungr, O., 2009. Characterization and numerical analysis of intermittent slope displacements and fatigue in deep-seated fractured crystalline rock slopes. *Proceedings of the 62nd Annual Canadian Geotechnical Conference*, Halifax.
- Wolter, A., Gischig, V., Stead, D., Clague, J.J., 2015w. Investigation of geomorphic and seismic effects on the 1959 Madison Canyon, Montana failure using an integrated field, engineering geomorphology mapping, and numerical modelling approach. *Rock Mech. Rock Eng.* (in review).
- Yin, Y., Wang, F., Sun, P., 2009. Landslide hazards triggered by the 2008 Wenchuan earthquake, Sichuan, China. *Landslides* 6, 139–151.